

DIRECT WRITING OF METAL FILMS VIA MICROPLASMA SCANNING AND
APPLICATION TO PRINTED SENSORS

by

Ahmed Magdy Elsayed Abdulwahed Ibrahim

B.Sc., Ain Shams University, 2013

A THESIS SUBMITTED IN PARTIAL FULFILLMENT OF
THE REQUIREMENTS FOR THE DEGREE OF

MASTER OF APPLIED SCIENCE

in

THE FACULTY OF GRADUATE AND POSTDOCTORAL STUDIES
(Electrical and Computer Engineering)

THE UNIVERSITY OF BRITISH COLUMBIA

(Vancouver)

February 2017

© Ahmed Magdy Elsayed Abdulwahed Ibrahim, 2017

Abstract

Direct writing of precise micro-patterns of metallic films is an emerging fabrication technique applicable for a vast range of devices. Techniques for printing various materials are being developed for some time owing to the escalating demand, and have seen substantial progress over the years. The objective of this research is to develop a simple direct writing technique that can accurately form desired patterns with high film quality, low cost, and rapid time. Micro glow discharge manipulation may be used to print metal structures with high precision. The proposed micro-scale process for local deposition and direct writing of metal films through sputtering of a micro-machined target electrode is achieved via a highly confined micro glow plasma generated between the electrode's end and the substrate without the need of processing under vacuum. Through the use of micro-machined cylindrical-shaped target electrodes of the desired metal or metal alloy, the microplasma is steadily sustained to confirm the local deposition of the electrode material on the conductive substrate. Film characterization, performed by thickness profilometer reveals the patterning of target material with thicknesses ranging from the 100-nm order to several micrometers, dependent on the discharge current and feed rate. The viability of the process to pattern films over non-planar surfaces is achieved with high quality. The applicability of the devised technique to micro-pattern T-type thermocouple junctions is demonstrated and the thermoelectric performance of the printed sensors is measured to verify their thermoelectric function, with a sensitivity of $39 \mu\text{V}/^\circ\text{C}$ that matches well the Seebeck voltage of a typical T-type device. The process scheme is promising for rapid, and low-cost production of thin film patterns and applicable to print of temperature sensors, potentially on a variety of objects including three-dimensional components and flexible substrates.

Preface

The work in Chapter 2 followed the prior study conducted in UBC Microsystems and Nanotechnology group at Takahata's Lab by Dr. Z. Xiao. I updated the experimental setup by adding the current regulating electronic circuitry and studied the process experimentally and theoretically in more depth. A part of the chapter (Copper deposition results) has been published in IEEE MEMS 2016 conference; A.M. Abdul-Wahed, A. L. Roy, Z. Xiao, and K. Takahata, "Direct writing of thin and thick metal films via micro glow plasma scanning," IEEE MEMS, 2016, pp. 443–446. Dr. Xiao did the experiments presented in Figures 3(a-b) and 4(a-b) in this paper. The preparation of copper electrodes was done by A. L. Roy. I conducted all the remaining testing and wrote most of the manuscript.

A version of chapter 3 has been presented in IEEE Sensors 2016 conference. [A.M. Abdul-Wahed], A.M. Abdul-Wahed, A. L. Roy, and K. Takahata, "Microplasma Drawing of Thermocouple Sensors," IEEE Sensors 2016, Orlando FL., 2016, pp. 1634-1636. I conducted all the testing and wrote most of the manuscript. The preparation of copper-coated glass substrates was done by the help of A. L. Roy.

Table of Contents

Abstract.....	ii
Preface.....	iii
Table of Contents	iv
List of Figures.....	vii
Acknowledgements	ix
Dedication	x
Chapter 1: Introduction	1
1.1 State of the Art Direct Writing Techniques	1
1.2 Research Goals.....	3
1.3 Glow Discharge	4
1.3.1 Discharge Voltage – Current Characteristics.....	4
1.3.2 Paschen’s Relation	5
1.3.3 Microplasma	7
1.4 Sputter Deposition	8
1.4.1 Diode Sputtering	8
1.4.2 DC Sputtering	9
1.4.3 Key Parameters of Sputtering Process	10
1.5 Thermocouples.....	11
1.5.1 Seebeck Effect in Thermocouples	12
1.6 Thesis Overview	13
Chapter 2: Micro Sputter-Deposition and Direct Drawing of Metal Films	15

2.1	Process Principle.....	15
2.2	Experimental Setup.....	17
2.2.1	Electrical Circuit.....	18
2.3	Experimental Results	20
2.3.1	Preliminary Test: Drawing of Thick Copper Film.....	20
2.3.2	Characterization of Drawn Thin Films	21
2.3.2.1	Effect of sputtering yield and threshold energy on the deposition process	22
2.3.2.2	Surface morphologies	23
2.3.2.3	Material composition	24
2.3.2.4	Dependence of patterns' geometry on process parameters.....	25
2.3.3	In-plane Patterning.....	32
2.3.4	Out-of-plane Patterning	33
2.4	Geometrical Impacts on Target Electrodes and Its Effect on Deposition.....	36
2.4.1	Electric Field Distribution with Flat and Tapered Electrode Bottoms: Finite Element Analysis.....	37
2.4.2	Static Mode Deposition.....	39
Chapter 3: Applications of the Direct-Writing Process - Printed Thermocouple		41
3.1	Fabrication Process	41
3.2	Fabrication Results.....	43
3.3	Test Setup and Preliminary Test Results of T-Type Thermocouples	46
3.4	An Approach towards a Fully Printed Micro-Thermocouple.....	49
3.4.1	DC Micro-Sputtering Deposition on Insulators.....	49
3.4.2	Preliminary Patterning Results	51

Chapter 4: Conclusion and Future Work.....	52
4.1 Summary of the Research.....	52
4.2 Future Work.....	53
Bibliography	56
Appendix A: Wet Potassium Hydroxide (KOH) Etching of Silicon.....	62

List of Figures

Figure 1-1 Patterning thin films by conventional photolithography techniques vs. direct writing.	2
Figure 1-2 Current versus voltage characteristic of Neon DC glow discharge [16].	5
Figure 1-3 Paschen's curve for air breakdown voltage [20].	6
Figure 1-4 Breakdown voltage against a range of gap spacing (μm) for air at 1 atmosphere [19]	7
Figure 1-5 Formation of the glow discharge inside a vacuum chamber to generate energetic particles [33]	9
Figure 1-6 Conventional DC sputtering system [33].	10
Figure 1-7 Illustration of the Seebeck effect [40].	12
Figure 1-8 Basic Thermocouple wire configuration.	13
Figure 2-1 Direct writing process	16
Figure 2-2 Experimental set-up for microplasma generation and manipulation for direct metal patterning.	18
Figure 2-3 Schematic of biasing circuit (Wilson Current Source) for the glow discharge.	19
Figure 2-4 Results of thick copper film patterning on silicon wafer.	21
Figure 2-5 Characterization results for direct patterning of copper thin film.	27
Figure 2-6 Characterization results for direct patterning of copper-tungsten thin film.	28
Figure 2-7 Characterization results for direct patterning of nickel 200 thin film.	29
Figure 2-8 Measured line width vs. discharge current with different scanning speeds.	30
Figure 2-9 Measured average thickness vs. scanning speed with different discharge currents.	31
Figure 2-10 Planar drawing of arbitrary pattern (letters "UBC").	32
Figure 2-11 Results of patterning copper film over nonplanar silicon substrates.	33

Figure 2-12 SEM images showing the possibility of patterning the electrode material over large silicon steps.....	35
Figure 2-13 Optical images of micro machined electrodes taken at specific periods of discharge	37
Figure 2-14 Finite element calculation of Electric Field between electrode and substrate	38
Figure 2-15 Results of static mode deposition.....	40
Figure 3-1 Fabrication steps of the thermocouple junction	42
Figure 3-2 Results of fabrication of the T-Type thermocouple junction	44
Figure 3-3 Results of Constantan drawing.....	45
Figure 3-4 Characterization results of Constantan linear patterns created using 80- μ m-diameter electrodes	47
Figure 3-5 Experimental set-up used to characterize printed micro thermocouples.	48
Figure 3-6 Measured thermocouple voltage as a function of temperature	49
Figure 3-7 Fabrication process of a fully printed thermocouple.....	50
Figure 3-8 Optical microscope image of a patterned structure.....	51
Figure A-1 Process steps of wet-etching of silicon with SU-8 mask.	62
Figure A-2 Process steps of wet-etching of silicon with PECVD silicon nitride mask.....	63

Acknowledgements

I offer my enduring gratitude to the faculty, staff, and my fellow students at the ECE department at UBC, who have inspired me to continue my work in this field. I owe particular thanks to Dr. Kenichi Takahata for being my supervisor and my mentor in this field. I wish to thank Anindya Lal Roy and Madeshwaran Selvaraj for helping me with my research from time to time, and more importantly for training me to use advanced equipment which facilitated the research I was doing. I wish to thank Zhimming Xiao, who helped in in the initial stages of my glow discharge research. I would like to thank the Faculty of Graduate and Postdoctoral Studies for their financial support including the Graduate Support Initiative award and the Josephine T. Berthier Fellowship. I wish to extend a very special thanks to my parents and friends for supporting me through my years of education. Finally, all praise is due to Allah, the Lord of the worlds.

“My Lord! Increase me in knowledge.”

Chapter 1: Introduction

Micro/Nano-patterning of metallic films is a primary requirement for micro/nano-manufacturing in a massive range of application areas including integrated circuits, micro-electro-mechanical systems (MEMS), sensors, biomedical devices, flexible electronics, and photonic integrated circuits (PIC). This necessity is commonly achieved through the use of planar fabrication techniques based on three main processes; material deposition in the form of thin film, lithography which transfers the desired pattern to the substrate by means of ultraviolet radiation or electron beams, and etching (excess material removal) processes. Even though this approach is highly applicable for wafer-scale production of planar devices, it naturally leads to time high cost because it implicates many process phases (film deposition, patterning using masks, and etching) which are time consuming, and requires complex high-vacuum equipment for plasma-based thin-film processing. While patterning of metal layers on non-planar surfaces is often required for microfabrication and packaging purposes (e.g., forming 3D micro coils [1, 2] and patterning interconnects over steps [3]), in the above application areas, this is not easily achievable through the conventional planar methods.

1.1 State of the Art Direct Writing Techniques

Scanning-mode “direct write” patterning of metallic thin films is a promising alternative approach to this requirement. As outlined in Figure 1-1, direct writing of thin films is a direct method to create the desired pattern without the need of conventional photolithography procedure, in which the film material is locally deposited on the substrate at the desired areas.

Previous work described various methods along this approach, including pulsed arc discharge [4, 5], microplasma jet [6], laser-assisted writing [7, 8], atomic layer deposition [9] and inkjet printing

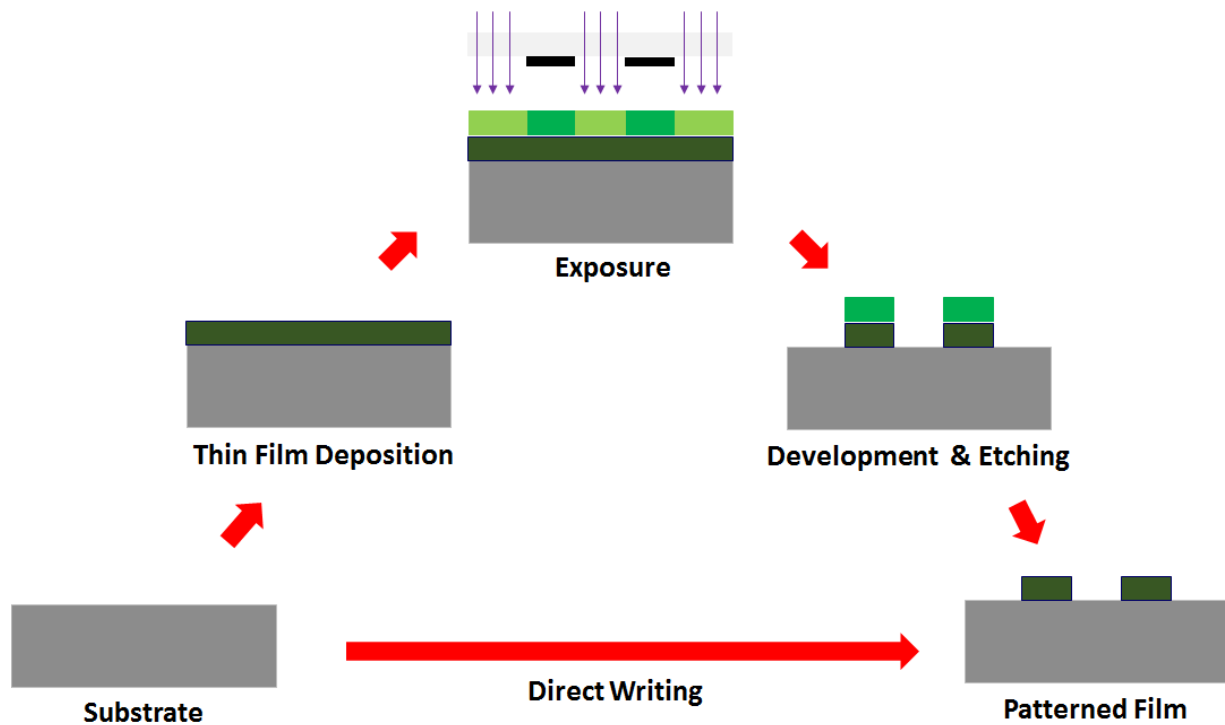


Figure 1-1 Patterning thin films by conventional photolithography techniques vs. direct writing.

[10]; nevertheless, most of them suffer a number of important concerns. Pulsed arc discharge systems were used to deposit copper lines [4] and form spiral structures [5]. Despite the system was relatively simple in [4], the material quality and film resolution were very low. J. Benedikt et. al. developed an atmospheric pressure microplasma jet for depositing hydrogenated amorphous carbon thin films from C_2H_2 gas [6]. However, in addition to the complex design of the plasma jet capillary, limitations of this technique includes the deposition on the capillary walls itself which results in dust formation and reduced ion energy that reduces the film quality. Several laser-assisted direct writing mechanisms have been reported [7, 8]. L. Wee and L. Li have used selective electroplating of copper electrolytic solution to form copper line. However, the use of a wet setup and laser source in [7] made the system's complexity very high. J. Chen et. al. used laser induced plasma to deposit thermoelectric misfit cobaltite thin films. Similar to the work of Wee and Li, the system is considered very complex and applicable to limited materials. An electron-beam induced

atomic layer deposition technique was developed to show direct writing of platinum patterns with high resolutions [9]. However, the process of ALD is very slow and this is known to be its major limitation. As outlined above, most of these techniques includes a number of essential issues, e.g., poor film thickness control, film quality and contamination, patterning resolution, and/or complex system configuration, to name a few. It is also worth noting that inkjet printing is a common path to direct writing of liquid-phase materials; for metal patterning, however, its use is limited to the deposition of metallic particles [10] – although continuous metal film could be formed via a post-deposition sintering process (to melt the deposited particles) [10], the need for high temperatures for this melting step also hinders the applicability of this approach.

1.2 Research Goals

In this research we aim to devise an alternative path to micro-scale local deposition of continuous metal film patterns. The process should be able to create the desired structures over both planar and non-planar surfaces to be applicable to a variety of applications. The desired process should be applicable to a wide range of materials and not limited to specific materials as in the techniques mentioned above. The system should be cost-efficient and simple; that is to say it shouldn't have complex vacuum systems, laser systems, or wet nature. Moreover, processing at atmospheric pressure is beneficial for vastly simplifying the system configuration and possibly achieving high deposition rates [11]. The potential applications of this process are printed sensors [12]. Temperature sensing is one of the promising areas in the field. This study explores an application of the developed direct write process to printed temperature sensors with a focus on micro thermocouples. In particular, drawing of Constantan (an alloy of 55% Cu and 45% Ni) on copper-coated glass substrates is investigated to form T-type thermocouple junctions.

1.3 Glow Discharge

In general, plasma may be defined as partially ionized gas made up of electrons, ions and neutral particles, but electrically neutral. Being electrically neutral, it contains equal quantities of electrons and ions and is, by definition, a good conductor. The word was first used by Irving Langmuir in 1928 to describe the ionized gas in an electric discharge [13]. Plasma is also considered the fourth state of matter. The term discharge was first used when a capacitor was discharged across the gap between two electrodes placed closed to each other. If the voltage is sufficiently high, electric breakdown of the gas occurs. The gas is ionized and the conducting path closes the circuit and a current can flow [14]. A glow discharge is a plasma formed by the passage of electric current through a gas. It is created by applying a voltage between two metal electrodes in a glass tube containing gas. When the voltage reaches the breakdown voltage, the gas in the tube ionizes, and begins conducting electricity, causing it to glow with a colored light that depends on the gas used.

1.3.1 Discharge Voltage – Current Characteristics

Vossen and Cuomo explained the DC discharge voltage-current relation [15]. The discharge that develops between the electrodes following breakdown has four main regions or states (Figure 1-2): Townsend region, Normal glow, Abnormal glow, and Arc. Initially, a few femto-amperes of current flows when a voltage is applied due to the presence of a small number of ions and electrons from some external source such as cosmic rays and natural radioactivity. The current is roughly constant because all the charges are moving. When the voltage is increased, charged particles acquire sufficient energy to produce more charged particles by collisions with the electrodes and neutral gas atoms. At the breakdown voltage, the current will increase by several orders of magnitude without a significant increase in voltage. This is called the *Townsend discharge*. As neutral gas atoms become charged ions (positively charged), they hit the cathode (negative

electrode) releasing secondary electrons, which form more ions by colliding with neutral gas atoms. These ions then return to the cathode producing more electrons that, in turn, produce more ions. This avalanche effect continues until the number of electrons generated is just sufficient to produce enough ions to regenerate the same number of electrons, which yields a self-sustaining discharge. The *normal glow* is the region when the gas begins to glow, the voltage drops, and the current abruptly rises to a nearly constant value. Additional pumping of power increases both the voltage and current in the discharge. This region, called the *abnormal glow*. When the current density increases further, electrons are emitted by a thermionic process and secondary electrons are emitted followed by further avalanche effect. Since the voltage is restricted by the output impedance of the supply, a low-voltage high-current *arc discharge* is generated.

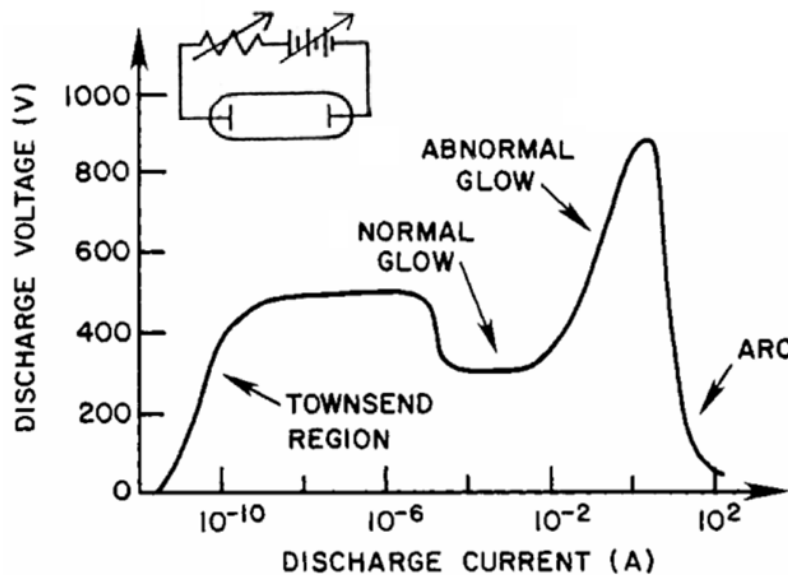


Figure 1-2 Current versus voltage characteristic of Neon DC glow discharge [16].

1.3.2 Paschen's Relation

Friedrich Paschen published what is currently known as Paschen's Law in 1889 [17]. The law briefly states that the breakdown voltage (V_{BD}) between two electrodes is a function of the product

of the gas pressure (P) and the separation gap (d) or the distance between the electrodes. Paschen's relation is given by:

$$V_{BD} = \frac{B P d}{\ln(P d) + \ln(A / \ln(1+1/\gamma))} \quad (1-1)$$

in which A , B , and γ are constants dependent on the specific gas between the electrodes [18].

Figure 1-3 shows the Paschen Curve for air, two flat parallel copper electrodes, separated by 1 inch, for pressures between 3×10^{-2} Torr and 760 Torr. At standard atmospheric pressure, $A = 11.25 \text{ m}^{-1} \text{ Pa}^{-1}$ and $B = 273.77 \text{ V/m Pa}$, and $\gamma = 0.01$ [19]. As shown in the plot, the breakdown voltage decreases with increasing Pd . The fact that the gas is not very dense or the electrodes are very close is (i.e. not enough neutral atoms exist to be ionized) is the reason for the high value of the breakdown voltage. As Pd increases, more neutral atoms exist and the breakdown becomes easier until it reaches a point where too many neutral atoms are present that increases the number of collisions of an electron before it reaches the anode. Hence, the electron needs more energy to make this journey and the breakdown voltage to ignite a discharge increases again.

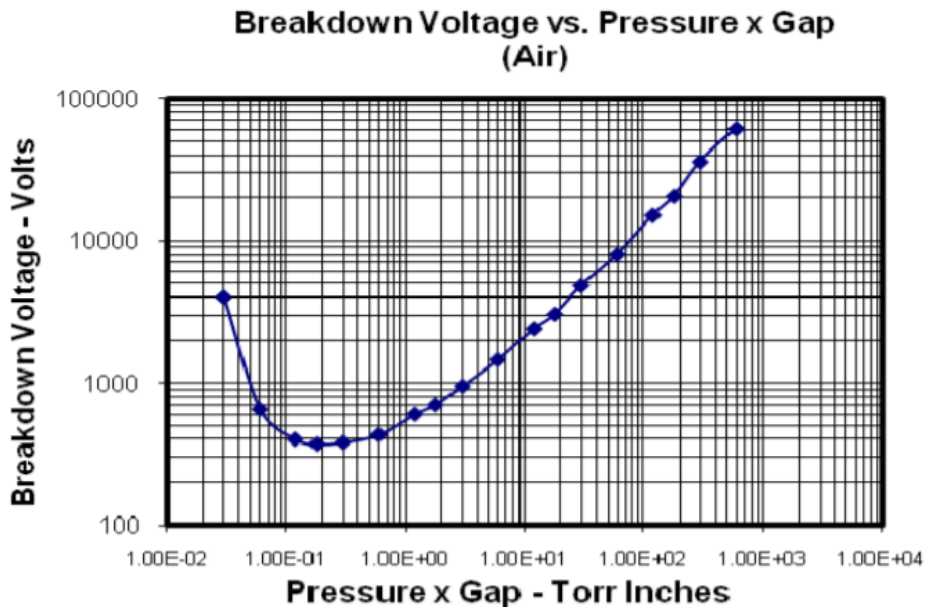


Figure 1-3 Paschen's curve for air breakdown voltage [20].

1.3.3 Microplasma

Microplasma is a plasma discharge of small dimensions in the order of ($\sim 10 - 1000 \mu\text{m}$). They can be generated at a variety of pressures. If the pressure of the gas between the electrodes increases, the gap between the electrodes must decrease to maintain the same breakdown voltage as indicated by Paschen's law. At values below 5 Torr cm, the discharges are called "pre-discharges" and are low intensity glow discharges [21]. Stable direct current atmospheric pressure plasmas can regularly be generated in air using microplasma systems. Figure 1-4 shows the breakdown voltage of air against the separation gap spacing at atmospheric pressure. Owing to the fact that the separation gap between the cathode and the anode is too small, the plasma can be sustained at low voltage levels (-200-300 V) at separation distances of 10-20 μm .

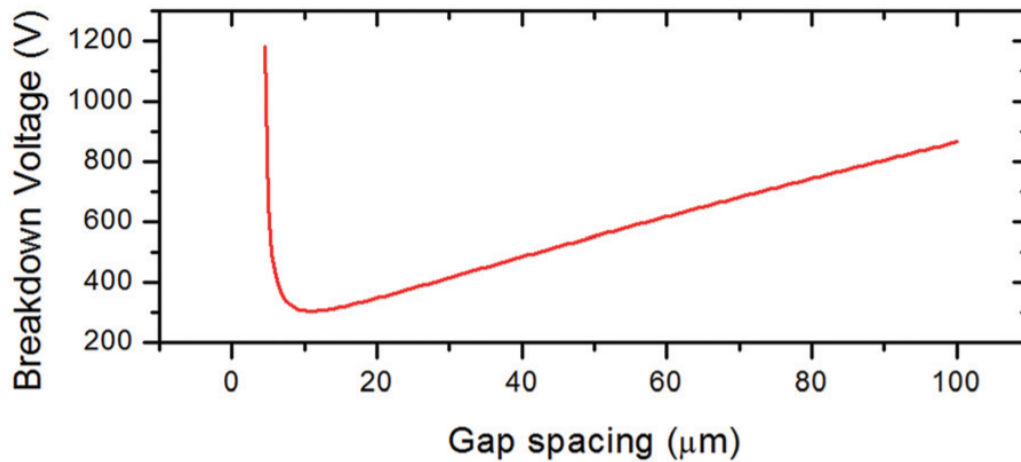


Figure 1-4 Breakdown voltage against a range of gap spacing (μm) for air at 1 atmosphere [19]

Nowadays, microplasma has a tremendous number of applications. Microplasmas have been used to enable the flat panel screen of a plasma display. The principle of operations relies on passing a high voltage through a gas generates an optical emission. Gary and Park are used microplasma for illumination [22]. Though confining plasmas in arrays of micro-cavities, thin and flexible light-

emitting sheets were successfully fabricated. Microplasma are also used to destroy volatile organic compounds such as benzene, heptane, octane, and ammonia in the surrounding air for use in advanced life support systems designed for enclosed environments [23]. Current research on the applications of microplasma includes nanomaterial synthesis and deposition [24, 25, 26, 27], gas and light detection sensors [28], as well as fuel cells [29].

1.4 Sputter Deposition

Sputter deposition is one of the popular physical vapor deposition techniques of thin films. It involves material removal from a solid surface as a consequence of momentum transfer between an energetic ion and the surface. When energetic ions (created in a plasma discharge or by a separate ion beam) are accelerated towards the target material, a plume of material is released. In a plasma discharge, the sputtering gas is often an inert gas such as argon or nitrogen. Reactive gases can also be used to sputter compounds. Sputtering can be used to deposit a wide range of materials including metals, metal alloys, and dielectrics.

1.4.1 Diode Sputtering

The simplest form of sputtering is the planar diode structure. The diode has two electrodes in which the target represents the cathode and the substrate is the anode, typically within a vacuum chamber. To achieve better film thickness uniformity, the target is disk-shaped and is placed at a distance from the substrate so that the flux of particles arriving at the substrate is more uniform [30]. The target is heated by the impact of ions, hence it is usually mounted to a water cooled backing plate or directly water [31].

There are three important sputtering techniques: DC diode sputtering, capacitive RF diode sputtering, and planar magnetron sputtering [32]. In diode sputtering, energetic ions created from

the discharged gas medium bombard the target and cause neutral particles to be ejected through momentum transfer. The ejected target particles fall on the surface of the substrate to form a thin film. The target acts as the cathode of the discharge, and is connected to either a DC negative voltage or RF signal, and the anode is usually grounded (or sometimes connected to a substrate bias). The power supply can either be a high-voltage DC power source or a high voltage RF source of a standard frequency of 13.56 MHz.

1.4.2 DC Sputtering

The DC plasma discharge creates the energetic ions, and can be created by applying DC voltage across electrodes in the presence of a gas at low pressure (Figure 1-5). In this process, the electric field formed between the electrodes will generate an electric current in the rarefied gas, due to the presence of electrons and ions formed by different processes (cosmic rays, thermionic emission ...etc.) [33]. The gas pressure shouldn't be very low to allow collisions between atoms and electrons before electrons hit the anode. The pressure should not be very high to let the electron reach enough velocity before it hits the atom [33]. Due to the electric field, ions reach the cathode with high energy so that they emit secondary electrons that moves towards the anode and generate

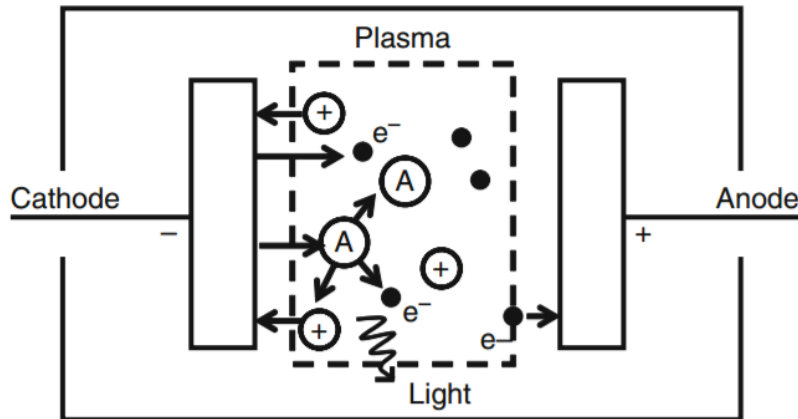


Figure 1-5 Formation of the glow discharge inside a vacuum chamber to generate energetic particles [33]

new collisions and sustain the plasma. At some ion energies, the ion can generate a series of collisions in the target leading to the ejection of materials. A typical DC sputtering system (Figure 1-6), contains the target electrode which is connected to a high negative voltage, and is cooled by water. The substrate is grounded or connected to a bias voltage to control the film properties [34]. The system is kept at controlled pressure and voltage. One of the main drawbacks in DC sputtering diode is that the cathode should be conductive.

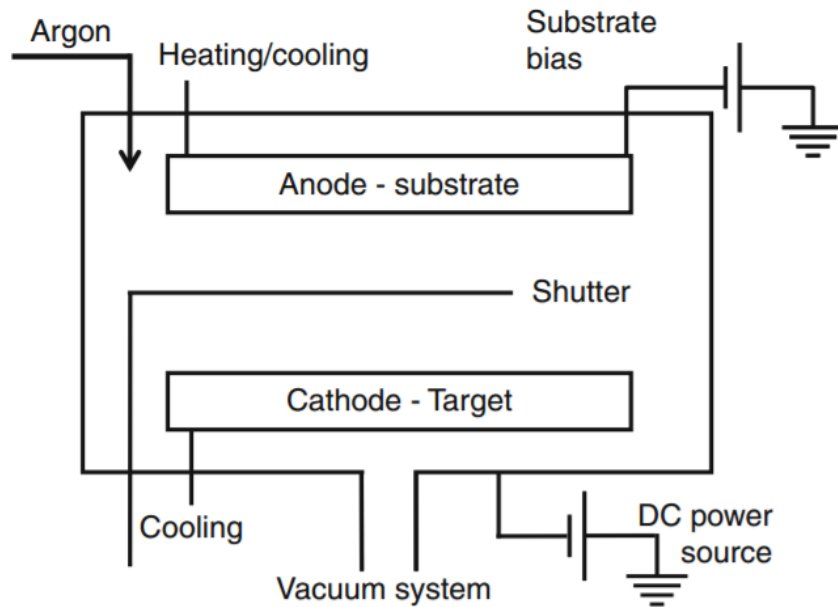


Figure 1-6 Conventional DC sputtering system [33].

1.4.3 Key Parameters of Sputtering Process

An important ratio to characterize the average electron/ion energy is the ratio of the electrical field intensity to the pressure [35]:

$$kT \approx \frac{E}{p} \quad (1-2)$$

where k is Boltzmann's constant, T is electrons/ions' temperature, E is the electric field intensity, and P is the pressure of the sputtering chamber. The higher the field intensity, the higher the velocity of free electrons/ions, but velocity is lost by inelastic collisions (with gas species) and

those collisions increases by increasing the pressure. Therefore at high gas pressures high voltage is required not only to breakdown the gas, but also to move the ions/electrons. The total bombarding flux of ions is then given by [35]:

$$J_{ion} = n_{ion} \mu_{ion} E \quad (1-3)$$

in which n_{ion} is the density of ions μ_{ion} is the ion mobility, and q is the charge of the ion, and the sputter rate is equal to the sputter yield (number of target atoms ejected per an incident ion) multiplied by the ion flux density:

$$r_s = Y J_{ion} \quad (1-4)$$

The sputtering yield depends on the ion incident angle on the target, the ion's energy, the atomic numbers and weights of the ion and target materials, and the surface binding energy of atoms in the target [36].

1.5 Thermocouples

Sensors are transducers that convert energy from one form to another. A thermocouple (TC) is a temperature sensor consisting of two dissimilar metal wires, joined at one end, and connected to a thermocouple thermometer or other thermocouple-capable device at the other end. When properly configured, thermocouples can provide temperature measurements over wide range of temperatures [37]. When two wires composed of dissimilar metals are joined at both ends and one of the ends is heated, a thermoelectric voltage is developed at the junction and there is a continuous current which flows in the thermoelectric circuit. Thomas Seebeck made this discovery in 1821 [38]. Thermocouples are inexpensive, and provide fairly accurate temperature measurements. Thermocouples can provide measurements in different environments, including fluid or toxic gas

environments. Thermocouple behavior can be explained by these phenomena: the Seebeck, Peltier, and Thomson effects [39].

1.5.1 Seebeck Effect in Thermocouples

A temperature difference between two points in space in a conductor or semiconductor material develops a potential difference between those two points [40]. This phenomenon is called “the Seebeck effect”. The value of the thermoelectric voltage (V_{TE}) developed for every unit temperature (T_j) difference is always referred as the Seebeck coefficient (S).

Considering a metallic wire that is heated at one end and cooled at the other (Figure 1-7), the heat at the first end makes electrons more energetic, and hence, they diffuse towards the cold part of the metal leaving positive ions behind them. The diffusion stops when the electric field due to positive ions becomes high enough to stop further immigration of electrons. The thermoelectric potential due to the electric field is called the Seebeck voltage [40]. The Seebeck coefficient is given by:

$$S = \frac{dV_{TE}}{dT_j} \quad (1-5)$$

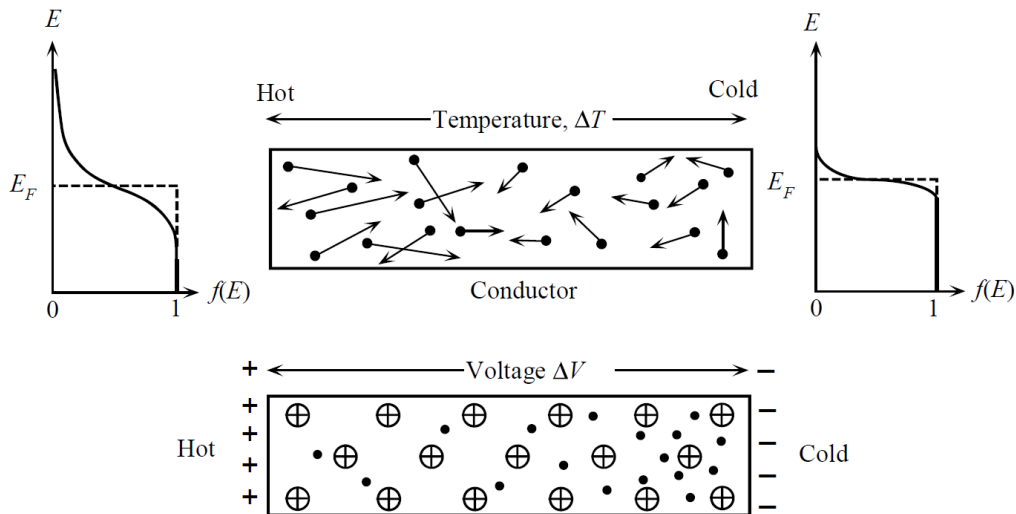


Figure 1-7 Illustration of the Seebeck effect [40]

A temperature gradient gives rise to electric potential difference.

If two wires of different materials are tied at an end and heated, while the other two ends are held cold as shown in Figure 1-8, the voltage due to the temperature gradient of the first wire will be different from the voltage of the other wire, and the potential difference across the two terminals is proportional to the temperature of the hot end. The thermoelectric voltage at the terminals is equal to the difference in Seebeck voltages of the two metals [37]. The Seebeck voltage of a given thermocouple wire pair can be measured by sweeping the temperature and recording the values of the thermoelectric voltage for every temperature while holding the voltmeter contact leads at the same temperature.

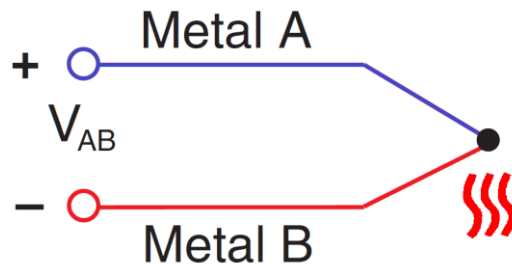


Figure 1-8 Basic Thermocouple wire configuration

1.6 Thesis Overview

In this chapter the motivation for the current work was presented. A brief history and the applications of direct writing methods were discussed. A technical background about glow discharges, gas breakdown, and microplasma was delivered. Sputter deposition was explained with focus on conventional DC diode sputtering, to provide a foundation for the research in this thesis. **Chapter 2** explains the principle of localized micro-sputter deposition of thin film and shows the experimental setup. Experimental results of deposition of three materials (pure copper, nickel 200 alloy, and copper-tungsten alloy) are shown. Patterning of arbitrary metal structures on planar surfaces and deposition on non-planar substrates are demonstrated. The effects of process

parameters on the deposited film properties are discussed in detail. **Chapter 3** presents the preliminary results of the fabrication and characterization of a printed thermocouple sensor for the T-type combination (based on copper - Constantan) as a potential application of the presented micro-sputter deposition process. **Chapter 4** summarizes the research and provides recommendations towards the improvement of the fabrication process to broaden the device applications realized by the proposed technique.

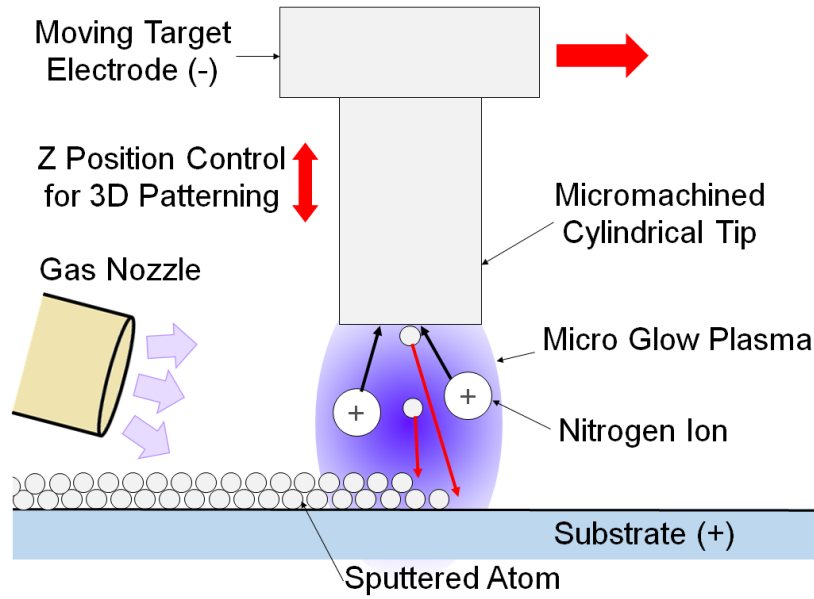
Chapter 2: Micro Sputter-Deposition and Direct Drawing of Metal Films

This chapter presents the first micro-scale process for local deposition and direct writing of metal films through sputtering of a micro-machined target electrode. The deposition process is achieved via a highly confined micro glow DC plasma generated between the electrode's tip and the substrate at atmospheric pressure. Using cylindrical electrodes with diameters down to 50 μm of three materials (copper, nickel, and copper-tungsten alloy), a micro glow plasma is stably established to show local deposition of the material on doped silicon. The controlled manipulation of microplasma enables direct writing of the target material, with variable pattern controlled by the discharge and scanning conditions. The feasibility of non-planar patterning is also demonstrated.

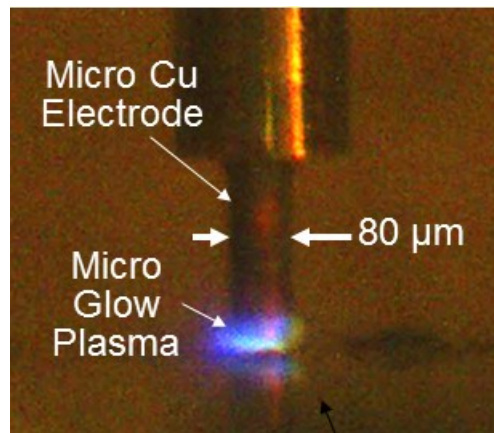
2.1 Process Principle

The concept of the new local deposition process is illustrated in Figure 2-1(a). The process principle is based on sputtering of a micromachined cylindrical electrode of the target material. Sputtering is performed via a micro glow plasma discharge established by applying a DC bias between the electrode tip and a conductive substrate. The discharge current is controlled by means of a current regulator inserted in the discharge circuit. In this diode system, the microelectrodes, with diameters down to 40 μm as tested in this study, act as the cathode while the substrates act as the anode. As illustrated in the figure, sputtering gas, nitrogen in this study, is supplied to the electrode tip, which is positioned above the substrate with a controlled gap separation, to sustain a steady micro glow discharge. The nitrogen ions created in the microplasma are accelerated towards the negatively biased anode by the electric field present across the gap space, bombarding and ejecting atomic-scale material from the bottom surface of the electrode. The ejected vapor-phase material is then deposited on the substrate surface to form a film locally. Film patterns with

arbitrary designs can be created through manipulating the electrode microplasma over the substrate laterally.



(a)



(b)

Figure 2-1 Direct writing process

(a) Conceptual diagram of the developed process (b) Optical image of the emission from a micro glow plasma established between a micro-machined copper electrode and a silicon substrate.

2.2 Experimental Setup

The custom-designed platform used for conducting experiments in this study is shown in Figure 2-2. The glow plasma is generated between a micro cylindrical target electrode and a doped silicon substrate (n-type with resistivity of 1-10 Ω .cm, unless otherwise stated) by applying a DC bias ranging from 200V to 500 V between them. To ignite the glow discharge, the electrode's tip is first positioned above the substrate with the gap distance noted above, and then the bias voltage is raised to a level that causes a gas breakdown, after which the voltage is set to a level suitable for the sputtering process. A current regulator is inserted in the discharge circuit as illustrated in Figure 2-2, so that a steady micro glow discharge is achieved. The mandrel and the substrate are kept in a transparent box to maintain the sputtering gas, with an oxygen sensor attached to ensure that the environment is fully filled with the gas. At a gas flow rate of \sim 200 sccm, the oxygen sensor's reading was zero indicating the chamber was full of nitrogen. The micro glow is sustained at a constant current in an approximate range of 0.3-4 mA for 50 μ m-diameter electrodes. The relative position of the electrode with respect to the substrate is controlled with a three-axis stage (A3200 Motion Controller, Aerotech Inc., PA, USA) with a nano-scale positioning resolution. The micro cylindrical electrodes of a target metal are prepared to have diameters of 35-260 μ m using a wire electro-discharge grinding technique [41]. The separation gap between the electrode tip and the substrate is adjusted to be 10-20 μ m. Using the set-up and conditions, a confined micro glow plasma is established at atmospheric pressure in a stable mode (Figure 2-1(b)) and can be manipulated by moving the electrode on the substrate while maintaining the defined discharge gap. Three materials were studied in details as target electrodes: pure copper, copper-tungsten alloy (75% tungsten, 25% copper), and nickel 200 alloy (99% nickel, with iron, molybdenum, silicon, copper, and carbon each less than 0.5%).

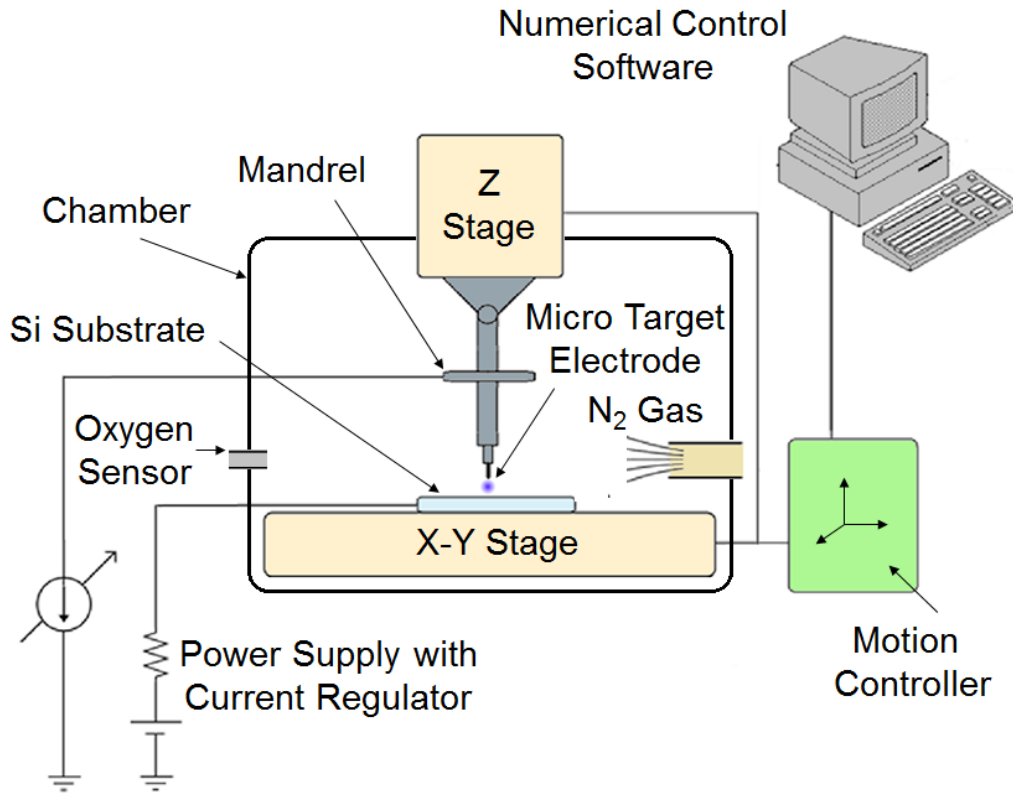


Figure 2-2 Experimental set-up for microplasma generation and manipulation for direct metal patterning.

The dependences of the local deposition and film patterning on the process parameters, including the discharge current, the scanning speed, and the discharge gap, are characterized using the set-up described above towards optimizing the process conditions for patterning tests. As will be discussed, controlling these parameters is revealed to enable fine tuning of the geometry (width and thickness) of the deposited metal pattern, offering a potential path to direct printing with varying dimensions without the need for changing the electrode tool.

2.2.1 Electrical Circuit

The stability of the discharge current is highly important to achieve a stable microplasma, a uniform deposition rate, and a higher-patterning resolution. Consequently, the use of a current regulator is recommended to sustain a stable discharge current. In the experimental setup, a Wilson current source circuit [42, 43, 44] comprised of high-breakdown voltage MOS transistors was used

for this purpose. The Wilson current mirror is a three-terminal circuit that inherently has a high output impedance to provide a stable output current regardless of the changes of the voltage at the output node. An input current at one terminal and provides an exact copy of that current at the output terminal. The mirrored current is a precise copy of the input current regardless the value of the voltage at the output terminal. To make use of the current mirror as a current source, a tunable input current is supplied at the input. As shown in Figure 2-3, the tunable current is obtained through the application of voltage across a 1 K Ω resistor from a tunable DC power supply. The current mirror is configured with 3 identical high power NMOS transistors as shown. A high voltage sufficient enough to breakdown the nitrogen gas is applied to initiate the glow discharge. Once the plasma is initiated, the circuit regulates the current so that the plasma is sustained stably at the desired discharge current value.

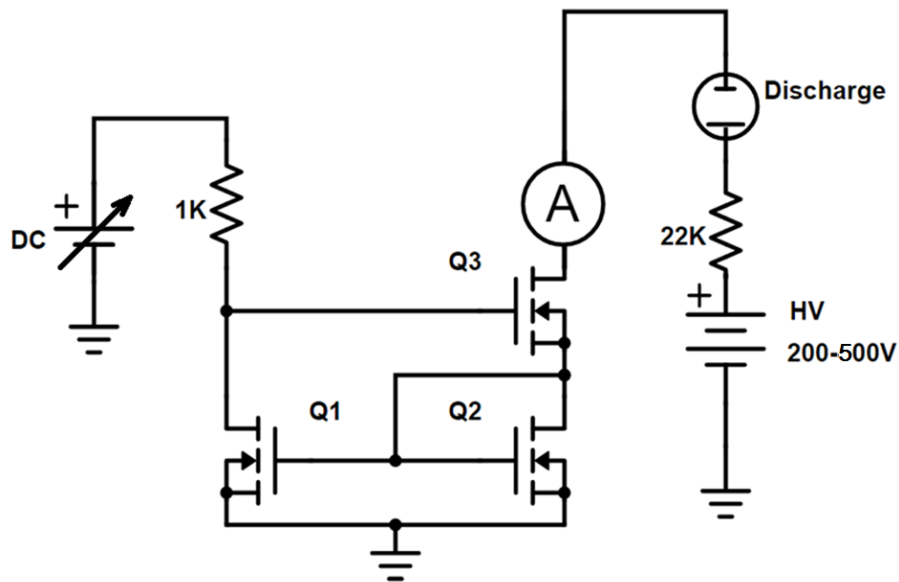


Figure 2-3 Schematic of biasing circuit (Wilson Current Source) for the glow discharge.

2.3 Experimental Results

Generating the microplasma between electrodes of different metals and the silicon substrates were confirmed. The micro-scale local deposition of thin films and arbitrary patterning of metallic microstructures on the substrates were successfully demonstrated. In this section, a preliminary test of drawing a thick copper film with thickness of $\sim 5 \mu\text{m}$ is presented. This is followed by characterization and demonstration of direct drawing of different materials (copper, copper-tungsten alloy, and nickel 200 alloy) patterned using 50- μm -diameter electrodes.

2.3.1 Preliminary Test: Drawing of Thick Copper Film

Sustaining microplasmas between moving electrodes of commercial copper wire and the silicon substrates, micro-scale local deposition and arbitrary patterning of copper film on the substrates were successfully demonstrated. Sample lines patterned using a 40- μm -diameter copper electrode is shown in Figure 2-4(a-b); this drawing was performed with a discharge current and a scanning speed of 0.8 mA and 20 $\mu\text{m/s}$, respectively. Figure 2-4(c) shows a transverse profile of another copper line printed using an 80- μm -diameter electrode with a larger current (3.6 mA) and a slower scanning speed (5 $\mu\text{m/s}$), indicating a film thickness of micron-scale thickness ($\sim 5 \mu\text{m}$). By programming the contour of the electrode's motion, arbitrary patterns could be created as displayed in Figure 2-4(d). The measurement of deposited film thicknesses, as shown in Figure 2-4(e), clearly suggests a trade-off relationship between the deposition thickness and the scanning speed (or the throughput) of the writing process. This is an expected outcome because, for a specific sputtering rate and a fixed discharge condition, the amount of material deposited within a small region along the scanning path should be more (or less) when the microplasma, the source of deposition, passes the region slower (or faster). The figure also shows that higher discharge currents led to larger thicknesses of the deposited film. This can be easily illustrated as

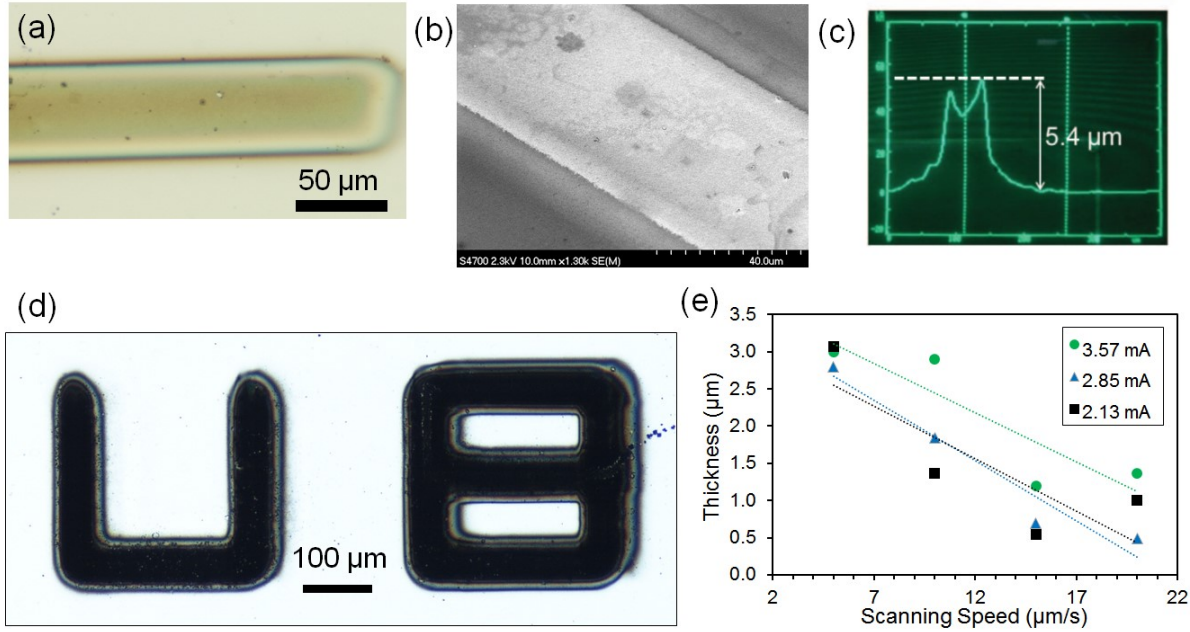


Figure 2-4 Results of thick copper film patterning on silicon wafer.

(a) and (b) Optical and scanning electron microscope (SEM) images of copper lines drawn with a 40- μ m-diameter electrode, respectively. (c) a sample cross-sectional profile of a patterned line showing \sim 5 μ m thickness (measured using a stylus profilometer Alpha Step 200, KLA-Tencor, CA, USA); (d) a demonstration of an arbitrary copper pattern drawing (performed using an 80- μ m-diameter electrode); (e) measured film thickness (peak value) vs. scanning speed with varying discharge currents tested using 100- μ m-diameter electrodes showing \sim 3 μ m film thickness.

at a higher discharge current, ions bombard the electrode with a higher density and thus eject more material from its surface to be deposited. The thickness was observed to change from \sim 200 nm up to 5.4 μ m by varying the current from 1.23 mA to 4.35 mA.

2.3.2 Characterization of Drawn Thin Films

In light of the application of the process for thin-film writing, the discharge current used in the further testing was limited to 1 mA or smaller towards controlling the film thickness in the nanometer scale. This experiment tested pure copper in addition to two alloys, copper tungsten

and nickel 200, as the target electrode materials. Examples of patterned lines of these materials using 50- μm -diameter electrodes of corresponding materials are displayed in Figure 2-5(a), Figure 2-6(a), and Figure 2-7(a) respectively. Both copper and copper-tungsten lines were deposited at a 0.4-mA discharge current, with scanning rates of 20 $\mu\text{m/s}$ and 5 $\mu\text{m/s}$, respectively. The nickel-200 line in the figure was patterned at a 0.6-mA discharge current and a 20- $\mu\text{m/s}$ scanning rate. The gap voltages for these conditions were measured to be similar (within a range of 380-400 V). All line patterns were created by scanning the electrode twice on the identical path in a reciprocating manner. The gap voltages for these conditions were measured to be similar (within a range of 380-400 V). All line patterns were created by scanning the electrode twice on the identical path in a reciprocating manner. The transverse profiles of each patterned line were measured at multiple locations with an equal (90 μm) interval using a stylus profilometer (DekTak XT 3D Profilometer, Bruker Co., MA, USA).

2.3.2.1 Effect of sputtering yield and threshold energy on the deposition process

The transverse profiles of each patterned line were measured at multiple locations with an equal (90 μm) interval using a stylus profilometer (DekTak XT 3D Profilometer, Bruker Co., MA, USA), and the results are shown in Figure 2-5(b), Figure 2-6(b) and Figure 2-7(b). The measured thicknesses of copper and nickel lines are approximately 130 nm and 85 nm on average (from Figure 2-5(b) and Figure 2-7(b) respectively). The average ion energy in a plasma can be characterized by the ratio of the electric field to the pressure [35], which is calculated to be in the order of ~ 100 eV for the process conditions used in this study. The sputter yields, γ , of copper and nickel with nitrogen ions are estimated (using the formula and material parameters reported in [36]) to be 0.30 atoms/ion and 0.19 atoms/ion, respectively, i.e., the ratio of the yields ($\gamma_{\text{copper}}/\gamma_{\text{nickel}}$) is 1.57. The deposition rate is proportional to the sputtering yield in theory, hence

the measurement of the thickness profile of copper and nickel lines (as shown in Figure 2-5(b) and Figure 2-7(b) respectively), showing thicknesses of approximately 130 nm and 85 nm, agrees well with the predicted sputtering yields (1.53). Pure tungsten has a small γ value (0.01 atoms/ion under the same conditions above); which in turns leads a tungsten-rich alloy has a low sputtering yield [45]. Patterning of the copper- tungsten alloy required to use 1/4 of the scan speed used for pure copper patterning to obtain a film thickness (\sim 200 nm, as in Figure 2-6(b)) comparable to that of the copper case – this condition clearly manifests the low total sputtering yield of the alloy. The experiments using the 50- μ m-diameter electrodes also revealed that the case of copper and copper-tungsten alloy could be deposited at a discharge current of 0.4 mA whereas the case of nickel required a slightly higher discharge current (of 0.5 mA) to initiate the deposition. This difference is likely associated with that in the threshold energy for sputtering, E_{th} , of the target materials, which is calculated to be 13.40 eV for copper and 16.84 eV for nickel [36] in the setting involved. Although the gap voltages of these two cases were measured to be almost identical as noted earlier, the process for nickel is presumed to have provided an increased ion energy led by a higher plasma temperature increases due to enhanced joule heating [46] to overcome the level of E_{th_nickel} . This hypothesis appears to be supported by the fact that the ratio of E_{th} for the two materials ($E_{th_nickel}/E_{th_copper} = 1.257$) matches very well with that of the discharge currents required for their depositions (0.5 mA/0.4 mA = 1.250).

2.3.2.2 Surface morphologies

The surface morphologies of deposited thin films were observed using a high-magnification SEM system (S3000N VP-SEM with EDX, Hitachi Ltd., Japan). The results indicated that the surfaces of the pure copper film produced (with 0.4-mA discharge current) was comprised of nanoparticles (\sim 50-nm in size) of the material with a good uniformity (as shown in Figure 2-5(d)), which is close

to the grain size of thin films deposited by conventional sputtering systems [47]. In the case of copper tungsten pattern produced (also with 0.4-mA current), the morphological features appeared to form coalesced nanoparticles (as shown in Figure 2-6(d)), resulting in a more connected thin film compared with the pure copper case. The interconnected nature of the film may be attributed to its increased thickness similar to the result reported in [48]. Nevertheless, the film morphology was found to be as uniform as the case of pure copper. Figure 2-7(d) shows that the nickel 200 alloy pattern produced (with 0.6-mA discharge current) exhibited a film that contained smaller particles with string-like nanostructures unlike the other two cases. The fact that a higher power was required to enable deposition of this material suggests that temperatures of the microplasma and the corresponding local region of the substrate were higher to provide higher ion energy [46, 49] and higher surface migration of landing atoms [50], respectively; these factors, along with the relatively lower deposition rate [51] of the resultant film (compared to the copper case), could have contributed to the smaller particles with smoother surfaces. The formation of the string-like nanostructures could be related to the buckling effect developed during the film deposition due to resultant residual stress [52] that might have been enhanced by the higher substrate temperature condition, especially at smaller film thicknesses that tend to allow deformation of the film easily [53].

2.3.2.3 Material composition

The material composition of the deposited patterns was analyzed using energy dispersive x-ray (EDX) spectroscopy (available with the SEM system used for the above observation). It was found from this analysis that the elements of the deposited thin films were well consistent with the electrode material used in each case as can be seen in Figure 2-5(c), Figure 2-6(c), and Figure 2-7(c) respectively. For pure copper (Figure 2-5(c)), the L and K peaks of the element are

clearly distinguishable the tungsten M and silicon K peaks are inherently too close (1.774 KeV and 1.74 KeV, respectively) to be distinguishable. However, the copper KA and tungsten L peaks are clear in the spectrum (at 8 KeV and 8.3 KeV, respectively), the ratio of their relative intensities were found to be nearly identical to those of the original target alloy (not shown), which suggest that the composition of the alloy elements was approximately preserved due to the fact that surface composition of the target electrode balances the difference in sputter yields [54] (for example, if more copper atoms were sputtered from the electrode (due to the high sputtering yield of copper) until the target's surface becomes rich in tungsten atoms, tungsten atoms will deposit until more copper is exposed). As can be seen in Figure 2-7(c), the result of nickel 200 alloy only revealed nickel signals due to the minimal amounts of the rest of the elements (including iron, molybdenum, silicon, copper, and carbon each <0.5%) included in the alloy. It should be noted that the silicon peak shown in these plots is due to the signals coming from the substrate. Low levels of oxygen seen in them could be due to the presence of native oxide on the substrate. The peak at ~3.5 KeV seen in all three materials is presumed to be a spectral artefact known as the sum peak (pile up) [55], which corresponds to a sum of two X-ray signals from silicon ($1.74 \text{ KeV} \times 2 = 3.48 \text{ KeV}$).

2.3.2.4 Dependence of patterns' geometry on process parameters

The geometry of the drawn films was evaluated by varying the process conditions, specifically the discharge current and the electrode's scanning speed. The measurement of deposited film thickness using the DekTak stylus profilometer revealed a dependence of the width of a printed line on the discharge current. Figure 2-8 show the results measured in the lines patterned using a 50- μm -diameter electrode with varying discharge currents under different scanning speeds, revealing an apparent dependence of the line width on the discharge current while indicating less dependence on the scanning speed. The dependence on the discharge current can be explained with an

observation that the lateral size of the microplasma (Figure 2-1(b)) was clearly modulated with discharge currents, e.g., increasing the input power enlarged the plasma size along the electrode's radial direction and thus caused a larger line width. Since a film pattern is defined by scanning the microplasma whose size can be electrically modulated, this observed dependence in turn offers a possibility to freely control the line width within a selected range (e.g., up to $\sim 30\ \mu\text{m}$, for the process with discharge currents up to 1.0 mA using 50- μm -diameter electrodes based on the results in Figure 2-8 during the patterning process. It can be also seen from these figures that with the smallest level of current, the produced line width matched well with the diameter of the electrode used (within a $\sim \pm 10\text{-}\mu\text{m}$ tolerance), representing a promising feature towards achieving precision patterning with the process. This result suggests that the resolution of the patterning process is effectively determined by the tip diameter of the micromachined electrode along with the smallest levels of discharge voltage and current that can sustain a stable microplasma and sputtering. The experiments also verified that the thickness and line width of the pattern was highly dependent on those two parameters (discharge current and scanning speed) as shown in Figure 2-9, with a tradeoff relationship between the deposition thickness and the scanning speed. These results are consistent with the thickness variation of thick films in Figure 2-4(d).

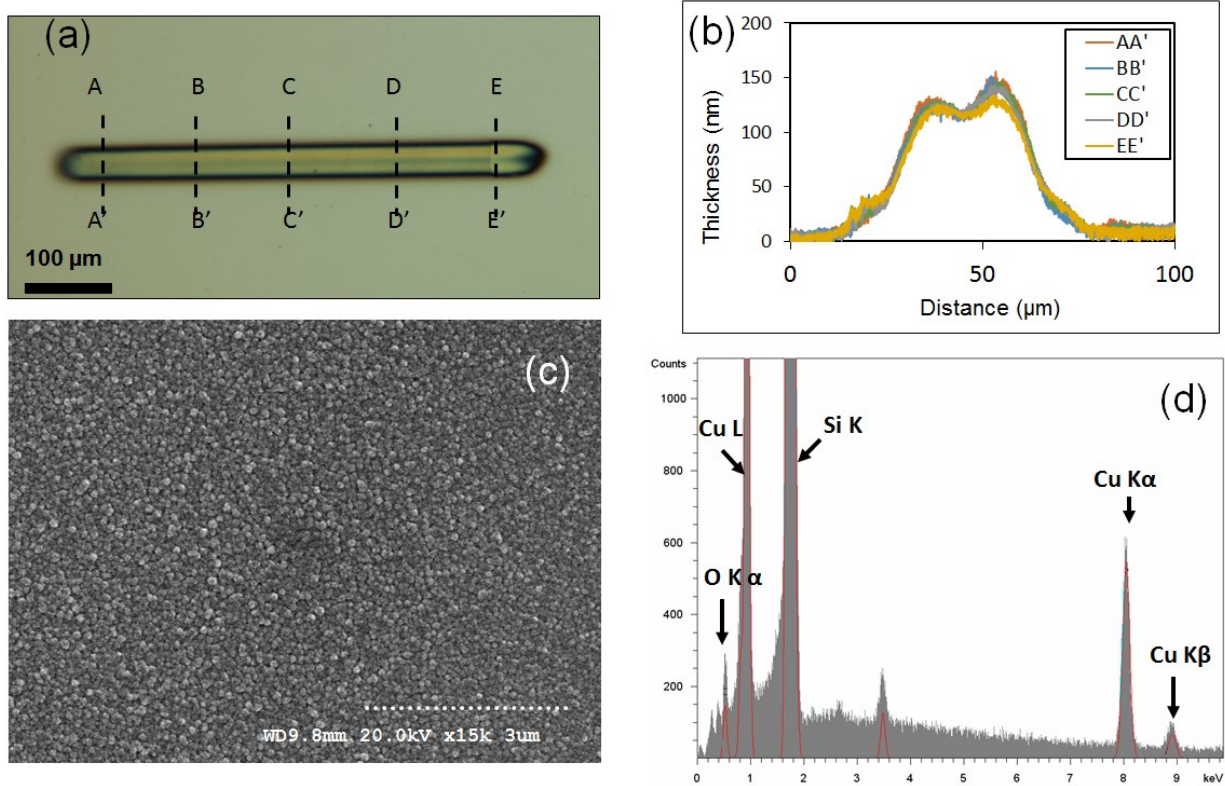


Figure 2-5 Characterization results for direct patterning of copper thin film.

(a) Optical image of a linear patter drawn with a 50- μm -diameter electrode at discharge current of 0.4 mA and scanning speed of 20 $\mu\text{m/s}$; **(b)** transverse cross-sectional profiles of the patterned line (measured at the locations indicated in the image in (a)); **(c)** close-up SEM image of the deposited thin film; **(d)** EDX signals obtained with created copper pattern.

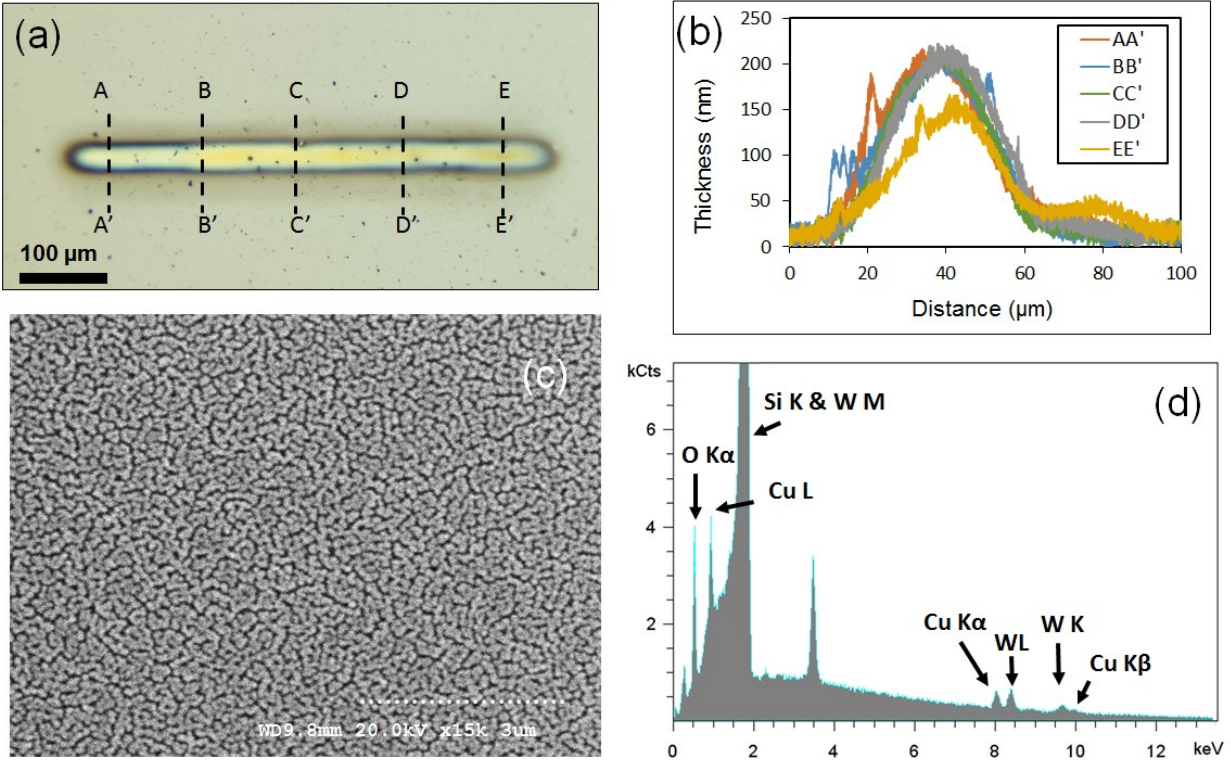


Figure 2-6 Characterization results for direct patterning of copper-tungsten thin film.

(a) Optical image of a linear patten drawn with a 50- μm -diameter electrode at discharge current of 0.4 mA and scanning speed of 5 $\mu\text{m/s}$; (b) transverse cross-sectional profiles of the patterned line (measured at the locations indicated in the image in (a)); (c) close-up SEM image of the deposited thin film; (d) EDX signals obtained with created copper-tungsten pattern.

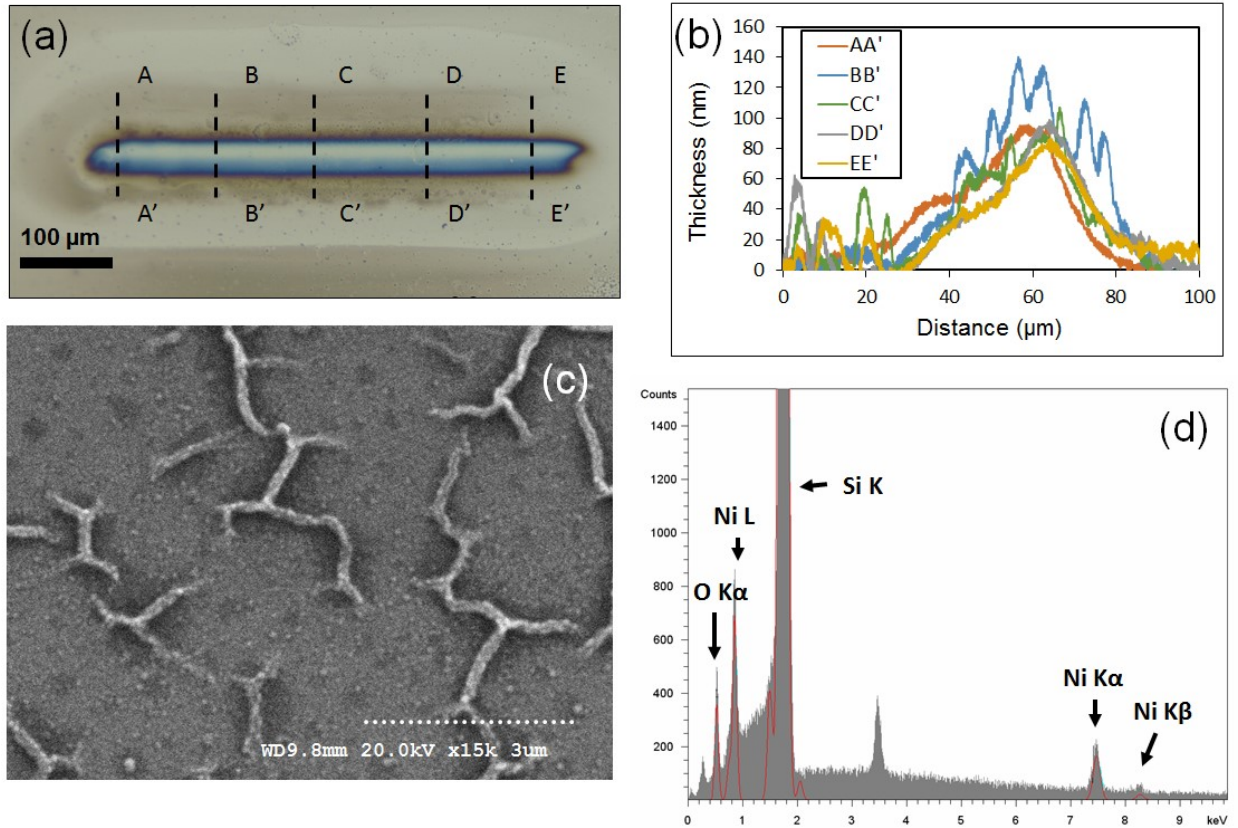
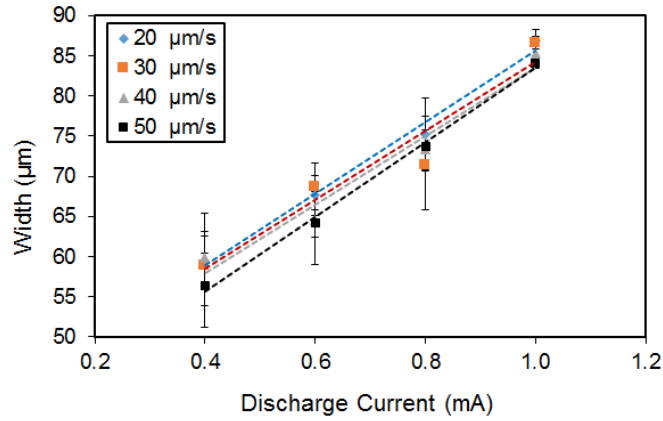
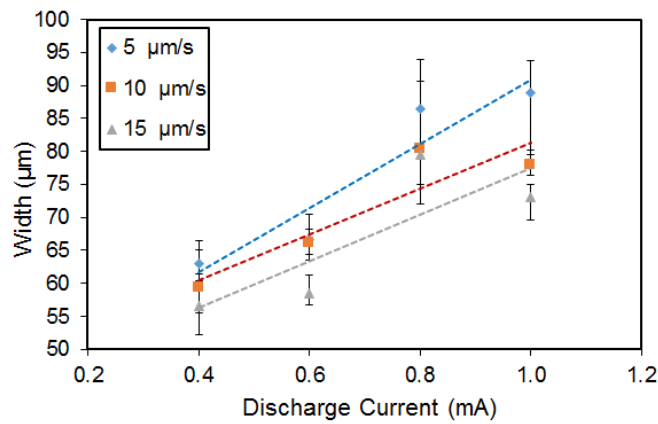


Figure 2-7 Characterization results for direct patterning of nickel 200 thin film.

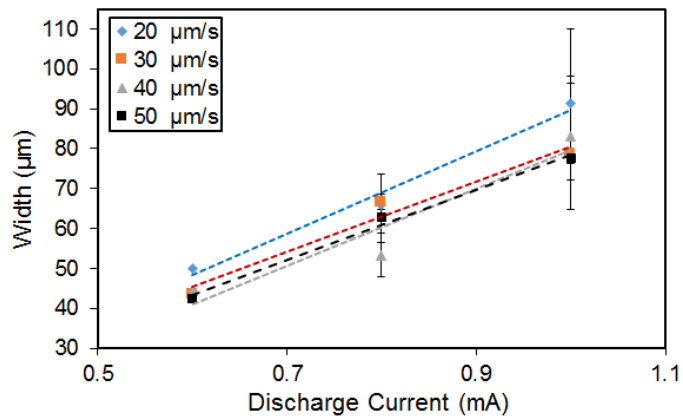
(a) Optical image of a linear patten drawn with a 50- μm -diameter electrode at discharge current of 0.6 mA and scanning speed of 20 $\mu\text{m/s}$; (b) transverse cross-sectional profiles of the patterned line (measured at the locations indicated in the image in (a)); (c) close-up SEM image of the deposited thin film; (d) EDX signals obtained with created nickel 200 pattern.



(a)



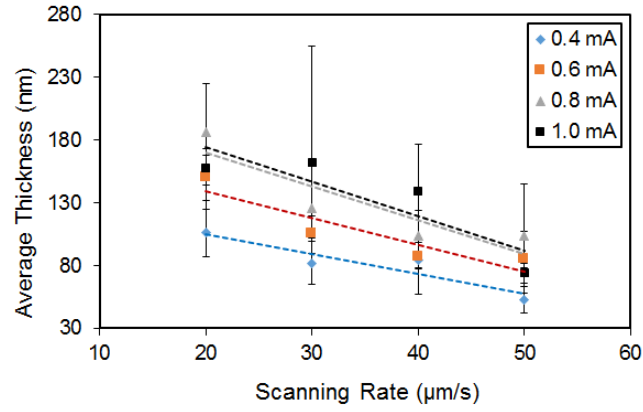
(b)



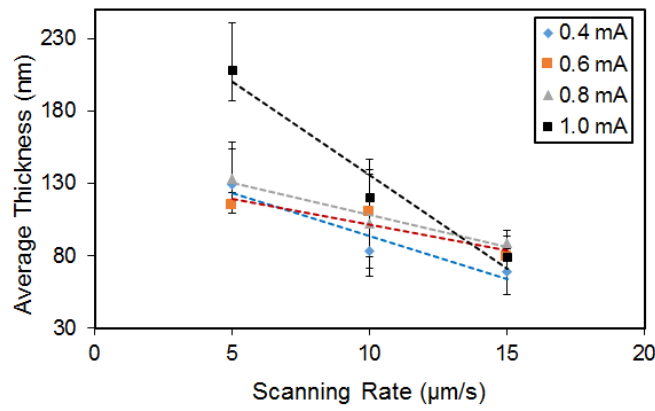
(c)

Figure 2-8 Measured line width vs. discharge current with different scanning speeds.

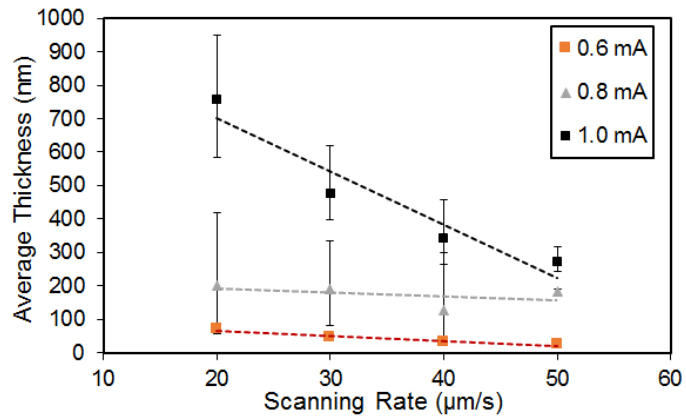
(a) Copper results (b) Copper-Tungsten alloy (c) Nickel 200 Alloy



(a)



(b)



(c)

Figure 2-9 Measured average thickness vs. scanning speed with different discharge currents.

(a) Copper results (b) Copper-Tungsten alloy (c) Nickel 200 Alloy

2.3.3 In-plane Patterning

Through programming the contour of the XY stage relative motion, arbitrary film patterns of the electrode material were successfully created. Figure 2-10(a-b) shows optical microscope images of in-plane patterns formed from copper and nickel, respectively, drawn on silicon substrates (p-type with resistivity of 0.001-0.005 $\Omega\cdot\text{cm}$) using 50- μm diameter electrodes by programmed motion of the XY stage. These patterns were drawn by scanning the electrodes back and forth along the contour with 20 $\mu\text{m/s}$ scanning rate at the smallest discharge currents required for these materials as noted earlier.. The SEM image in Figure 2-10(c) demonstrates the ability of to reproduce same patterns. The material in the figure was copper.

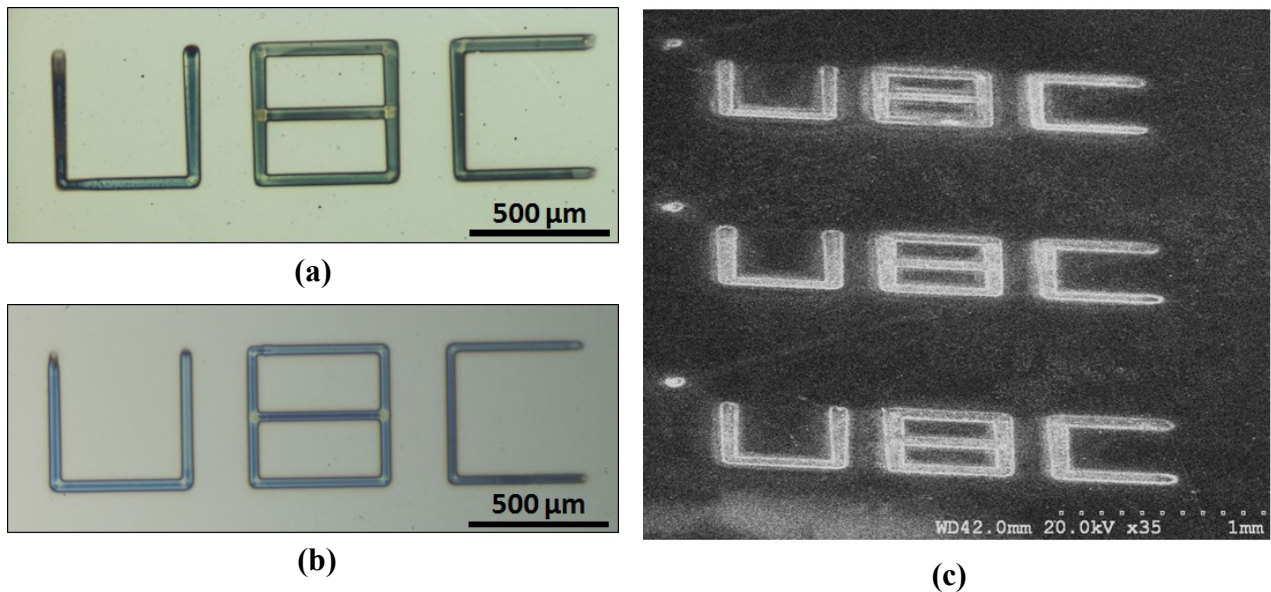


Figure 2-10 Planar drawing of arbitrary pattern (letters “UBC”).

Optical images of (a) copper and (b) nickel 200 patterns created on silicon; (c) SEM image of an array of copper patterns consecutively drawn on the substrate using the identical micro electrode of copper. The silicon used for this experiment was highly doped p-type (resistivity 0.001-0.005 $\Omega\cdot\text{cm}$).

2.3.4 Out-of-plane Patterning

The demonstrated process is potentially applicable to direct metal writing over 3D structures beyond the aforementioned planar patterning, through out-of-plane electrode scanning with synchronous multi-axes control. As displayed in Figure 2-11(a-b), deposition of lines over $\sim 10\text{-}\mu\text{m}$ silicon steps and along the side walls was successfully achieved using a $50\text{-}\mu\text{m}$ diameter electrode at microplasma current of 0.4 mA , scanned twice at $20\text{ }\mu\text{m/s}$ speed. In this test, the silicon steps were prepared by anisotropic wet etching in potassium hydroxide solution – details of this process are given in Appendix A. In Figure 2-11(a), the electrode was laterally approached to the step while maintaining a microplasma on the higher plane of the substrate; when it reached the etched part of the silicon, the electrode was then moved along an inclined path

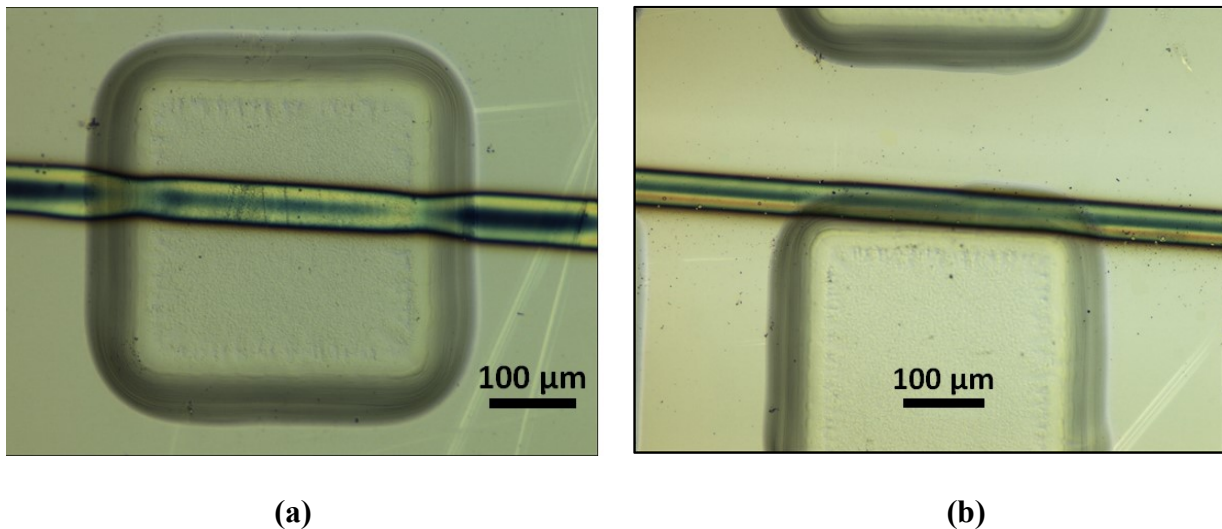


Figure 2-11 Results of patterning copper film over nonplanar silicon substrates.

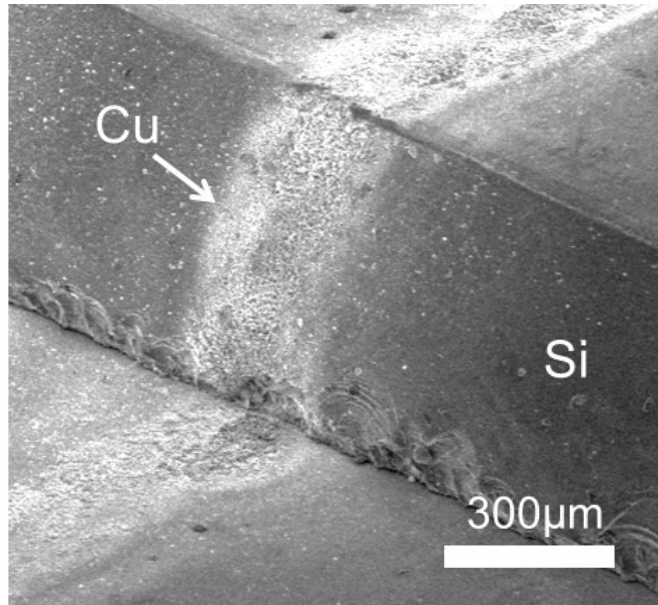
(a) Deposition across a square pattern etched in silicon using KOH with depth $10\text{ }\mu\text{m}$ (b) deposition on the side walls of a KOH etched silicon substrate.

parallel to the side walls (111 plane) while sustaining the plasma at the same discharge current, after which it was again laterally scanned on the lower substrate to continue drawing until it

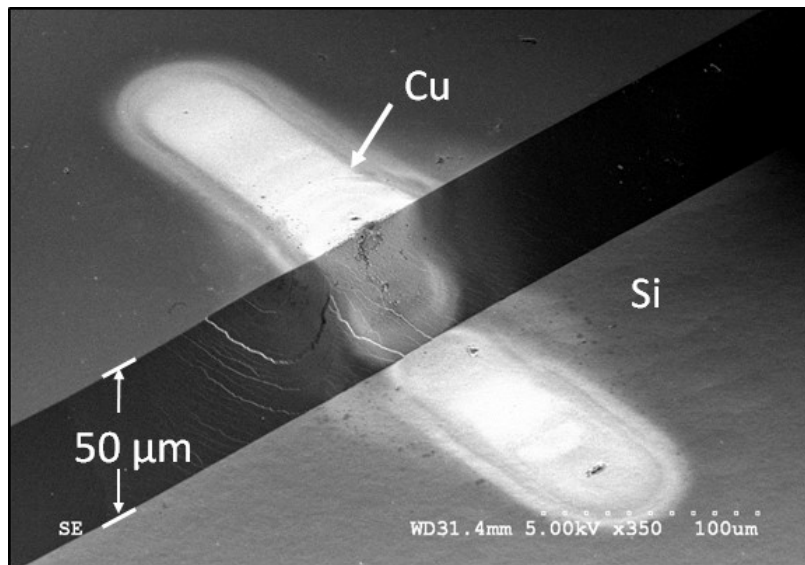
reached the next step. In Figure 2-11(b), the electrode was slightly lowered to maintain the plasma discharge stable between the electrode and the inclined 111 plane.

Moreover, the deposition over large steps (relative to electrode dimensions) was explored. As a preliminary test to evaluate this feasibility, film drawing was performed over large steps made on the silicon substrate (prepared by bonding a 500- μm -thick piece of the same silicon). As can be seen from a sample result shown in Figure 2-12(a), out-of-plane drawing was indeed feasible. In this test, the electrode was laterally approached to the 500- μm -tall step while maintaining a microplasma on the lower substrate; when it reached a 10-20 μm distance from the step, the microplasma emerged between the side of the electrode and the step's sidewall, which apparently contributed to the deposition on the sidewall. The electrode was then pulled up over the step while sustaining the side plasma, after which it was again laterally scanned on the upper substrate to continue drawing with the microplasma created on the electrode's bottom.

In addition to wafer bonding, silicon steps with vertical depth of 50 μm prepared by anisotropic wet etching similar to the case in Figure 2-11 (refer to Appendix A). At a scanning rate of 20 $\mu\text{m}/\text{s}$ and a discharge current of 0.4 mA, a copper electrode was scanned back and forth across the nonplanar silicon substrate to draw a line over a step as shown in Figure 2-12(b). It is worth noting that the lines drawn over the steps exhibited certain variations in their widths, as can be seen in Figure 2-12(b). In particular, the line width appears to become greater at a convex corner and vice versa at a concave corner. This outcome could be related to a combination of the following two factors: 1) the field intensity rises at a convex corner to enhance the sputtering deposition whereas the opposite phenomenon occurs at a concave corner, and 2) the minimum distance between the electrode surface and the substrate surface increases near a concave corner to lower the deposition



(a)



(b)

Figure 2-12 SEM images showing the possibility of patterning the electrode material over large silicon steps
(a) A preliminary result from direct writing of Cu on Si over a 500-μm step, performed via out-of-plane position control of the microelectrode with respect to the Si surfaces. (b) deposition of a copper line over a KOH etched silicon substrate with vertical depth of 50 μm.

rate on that region. This variation in linewidth becomes more apparent in the case of patterning using smaller diameter electrodes (as can be seen from a comparison between the results between Figure 2-12(a) and 2-12(b)). Nevertheless, it was indeed verified that the process was capable of printing continuous patterns over bulk-micromachined steps, indicating the feasibility of printing patterns of thin metal film on 3D structures through the developed process. The mask-less, direct-writing ability is expected to offer a wide range of applications where conventional photolithography-based approach is not effective.

2.4 Geometrical Impacts on Target Electrodes and Its Effect on Deposition

The profile of the thin film cross section is one of the important parameters to test the process performance and process quality. Moreover how the target electrode is consumed determines several process aspects including optimum electrode geometry and life time of the target. It was found that the cylindrical target microelectrodes formed rounded tips after certain time with minor changes in pattern geometries. In light of this, the geometrical dependence of the electrode on the process time was studied experimentally. For this experimental characterization, the microelectrodes of copper and nickel were scanned at a rate of 20 $\mu\text{m/s}$ for a distances of 3mm and 6mm with a microplasma generated at a discharge current of 0.5 mA, after which the resultant shapes of the electrodes were observed using a measuring microscope. As can be seen in Figure 2-13(a-b), the consumption at the corners of the cylindrical-shaped electrode was greater than the bottom when it was used for a certain period, leading to form tapered sidewalls with time. This observation also indicates that copper was consumed more than nickel; this outcome can be interpreted by the fact that the sputter yield of copper is lower than that of nickel [36].

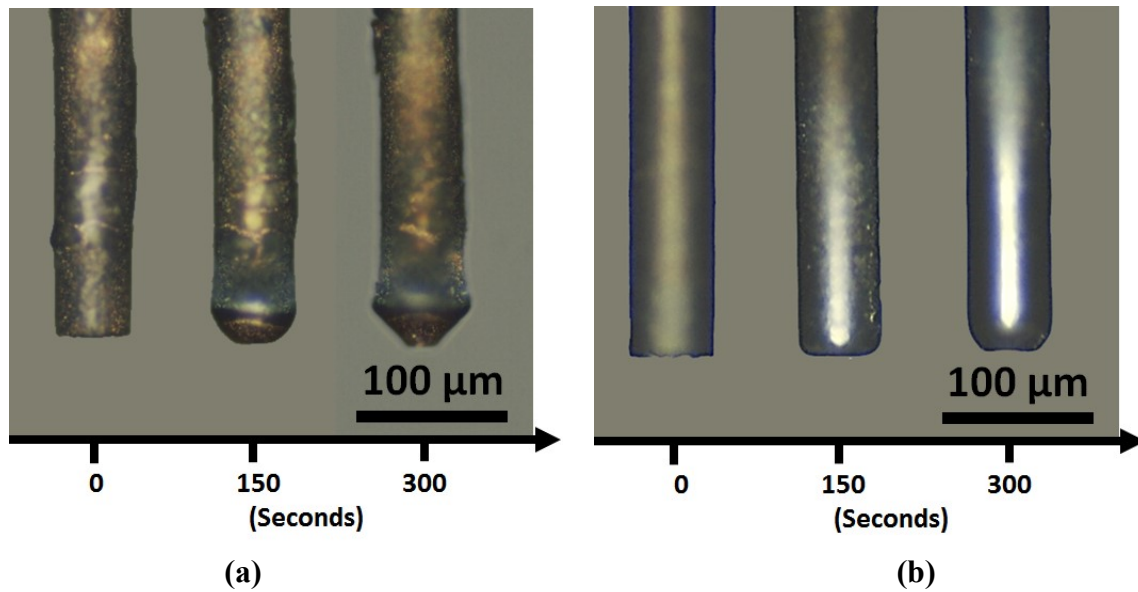


Figure 2-13 Optical images of micro machined electrodes taken at specific periods of discharge
 (a) Copper Electrode (b) Nickel Electrode

2.4.1 Electric Field Distribution with Flat and Tapered Electrode Bottoms: Finite Element Analysis

In the microplasma, the trajectory of nitrogen's positive ions follows the electric field lines towards the negatively biased target electrode. The distribution of the electric field determines which parts of the electrode will be attacked more/less by the kinetic positive ions. Atmospheric pressure microplasmas are inherently weakly ionized [59]. Therefore, when calculating the electric field distribution at the surface of the electrodes (not in the plasma itself), the electromagnetic fields due to motion of plasma charged particles can be neglected. The electric field distribution due to a voltage applied between a 50- μm -diameter electrode and the substrate (with a gap of 20 μm) was calculated through finite element analysis using COMSOL Multiphysics® (version 5.2). The result show the peaks of the field at the corners of the electrode profile with the intensity level approximately $3.5\times$ greater than that at the center of the bottom surface (Figure 2-14(a) and 2-14(c)). This field concentration consequently results in a higher consumption rate of electrode

material at the corners compared with that at the bottom's flat region, approaching towards a tapered profile as experimentally observed (Figure 2-13). Considering this consumption effect, the electric field was recalculated for a tapered-cylindrical electrode tip with top diameter of 50 μm , a smaller bottom diameter of 25 μm and a tapered length of 20 μm . The result displayed in

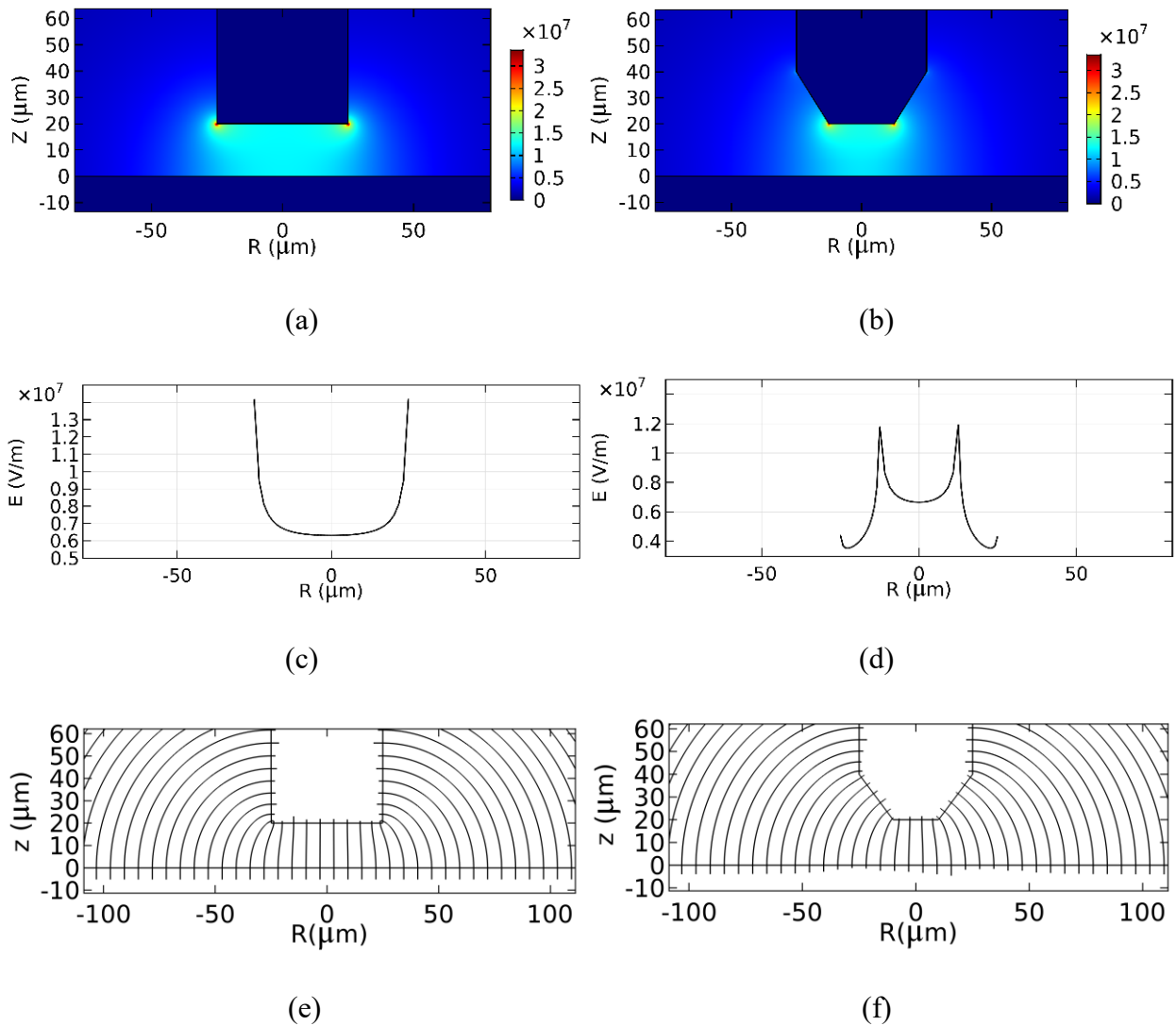


Figure 2-14 Finite element calculation of Electric Field between electrode and substrate

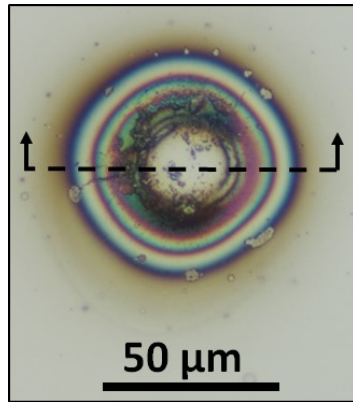
(a-b) Distribution of the electric field intensity of perfect cylinder and a tapered electrode respectively
(c-d) electric field intensity at the bottom surface of the electrodes (e-f) Streamline plot

Figure 2-14(b) and 2-14(d) indicates that the maxima of the electric field intensity are located at the edges on the flat bottom surface and the peaks of the field are still in the same order of

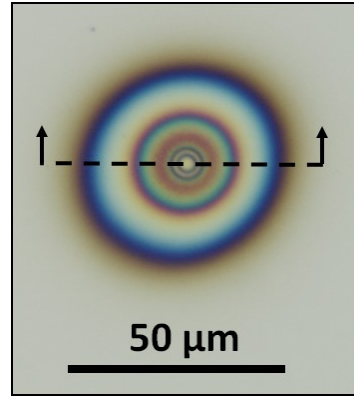
magnitude. To visualize the reason of higher field intensity at the corners, the streamline 2D field patterns are plotted to show more lines at the corner points (Figure 2-14(e-f)).

2.4.2 Static Mode Deposition

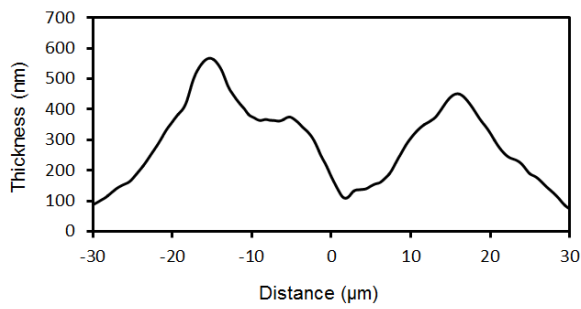
Figure 2-15(a-b) show the deposited films by sputtering tapered nickel electrodes (50- μm -diameter cylinders) that were held stationary during the deposition process (for \sim 5-10 seconds). The cross-sectional profiles of the deposited spots (measured along the broken lines shown in Figure 2-15(a-b) using the stylus profilometer) are plotted in Figure 2-15(c-d), respectively. The thickness dips in the central region of the profiles in Figure 2-15(c-d) could be caused by the low sputtering rate at the middle of the electrode if compared to the sides. It is evident from Figure 2-15 that as the electrode is consumed to have a tapered bottom surface, the diameter of the deposited film narrows, and consequently, the line width is reduced when a pattern is drawn. This size reduction can be explained by narrowing of the distance between the two field peaks as indicated in Figure 2-14(c-d). This effect may be compensated by increasing the discharge current so that the plasma size increases and the line width increases as demonstrated in section 2.3.2.4.



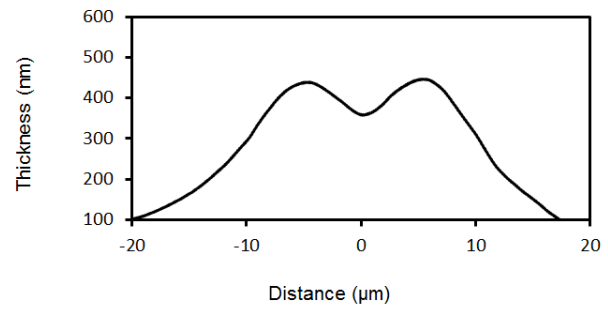
(a)



(b)



(c)



(d)

Figure 2-15 Results of static mode deposition

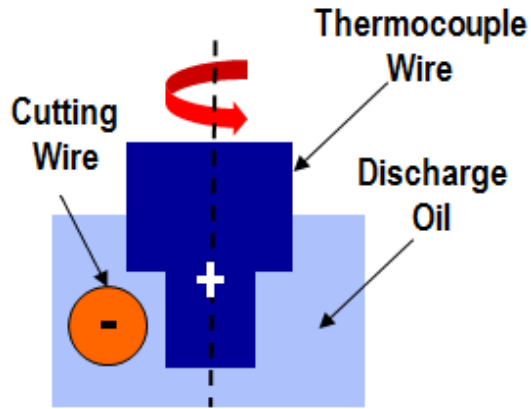
(a-b) Optical microscope images of deposited spots through sputtering stationary nickel electrodes consumed with prior processing for ~600 seconds and ~1200 seconds, respectively.

Chapter 3: Applications of the Direct-Writing Process - Printed Thermocouple

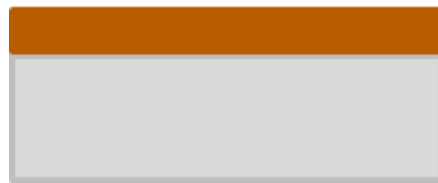
One potentially promising application of the presented micro-sputter deposition process is rapid, low cost production of printed temperature sensors such as thermocouples and resistive temperature detectors [60, 61]. In particular, micro thermocouples could be printed using commercially available thermocouple alloy wires as the sputtering targets in the process. This ability will allow micro printing of standard type thermocouples directly on arbitrary objects (e.g., mechanical/fluidic parts/tubes and minimally invasive smart implants) that require temperature management but cannot accommodate separate sensors with them. This chapter reports the preliminary results from the experiments done on the formation of micro thermocouples via the above process. The particular focus is placed on drawing of Constantan (an alloy of 55% Cu and 45% Ni) for T-type thermocouple printing. The T-type thermocouple is capable for measurements from -200 to 350 °C. Both conductors have stable characteristics since both of them are non-magnetic, hence there is no Curie point.

3.1 Fabrication Process

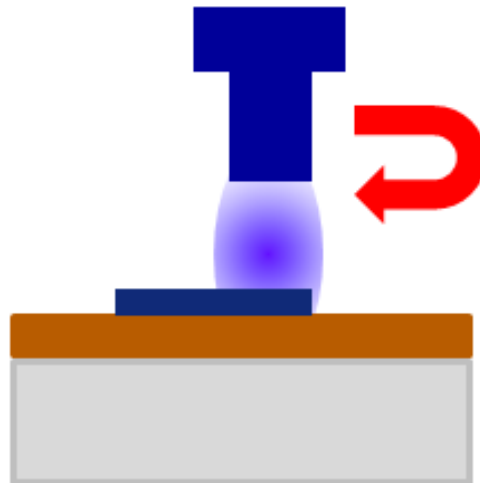
The fabrication process of the thermocouple devices, shown in Figure 3-1, involves three main processing steps: firstly, cylindrical target electrodes of the thermocouple grade Constantan alloy (55% Cu, 45% Ni), are cut by means of wire electro-discharge grinding. The target alloy is made of a commercially available T-type thermocouple wire (AWG 30). Secondly, a copper layer of thickness of $400\text{-}\mu\text{m}$ is evaporated on a glass substrate using an electron-beam evaporator to create the first material of the thermocouple junction. The copper layer acts as the anode of the diode sputtering micro-reactor. Finally, for localized sputtering deposition of a thermocouple alloy, a micro glow plasma is generated between the micromachined cylindrical electrode of the alloy and the copper layer on the glass substrate, and the Constantan



(a)



(b)



(c)

Figure 3-1 Fabrication steps of the thermocouple junction

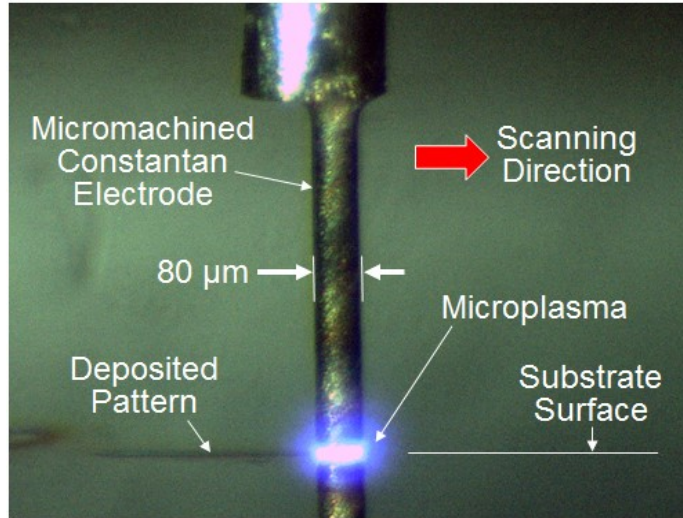
(a) Preparation of the sputtering target (Constantan wire) using wire-electro-discharge grinding, (b) e-beam evaporation of copper layer on a glass substrate, (c) micro-sputtering of the target and scanning it back and forth to draw the thermocouple junction.

film patterns are created by manipulating the electrode-microplasma over the substrate laterally. The diameters of the target electrode used are 50-80 μm . The localized deposition of the Constantan alloy on the copper layer forms a T-type thermocouple junction. Lines were patterned by scanning the microplasma twice along the same track (via a reciprocating motion) to enhance uniformity of the pattern shape.

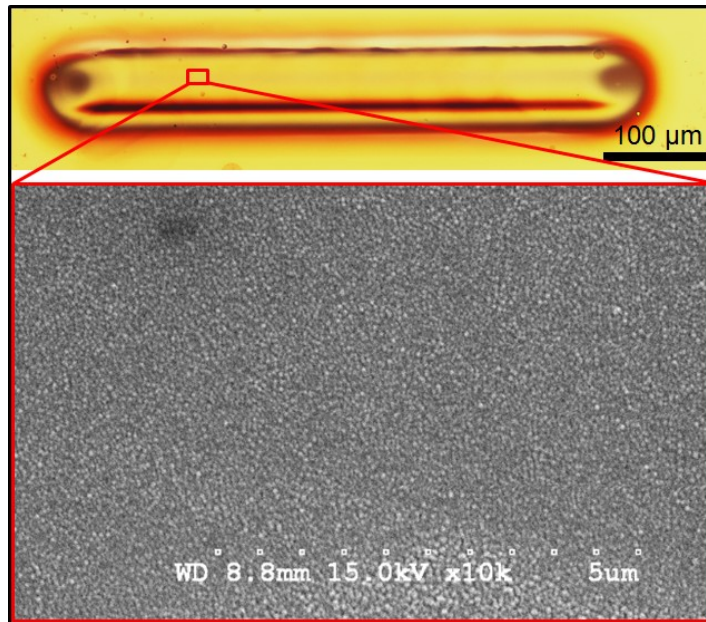
3.2 Fabrication Results

Similar to what was demonstrated in Chapter 2: The micro glow plasma was verified to stably sustain on the electrode with discharge gaps of ~ 10 μm and deposit the material locally in both static and scanning modes. The optical emission of the plasma from an 80- μm electrode is shown in Figure 3-2(a). A linear pattern of Constantan drawn using a 50- μm -diameter electrode (at a plasma current of 0.4 mA and a scanning rate of 20 $\mu\text{m}/\text{s}$) is shown in Figure 3-2(b). The constantan pattern is well defined on the copper-coated substrate. The figure also shows the surface morphology of the surface of deposited Constantan that appears to be covered by nanoparticles (~ 50 -nm in size) with a high uniformity. The result in Figure 3-2(b) agrees well with the pure copper case discussed in Figure 2-5(c).

Arbitrary patterning of Constantan film on the copper-coated substrates was successfully demonstrated by scanning the micromachined Constantan electrode; one example shown in Figure 3-3(a) displays an array of 500- μm -long lines of Constantan film patterned using an 80- μm -diameter electrode. Each line was patterned by scanning the microplasma twice along the same track. The cross-sectional profiles of patterned lines were characterized using the DekTak stylus profiler, revealing that their thicknesses were in the order of 100 nm (Figure 3-3(b)) and varied depending on the process conditions.



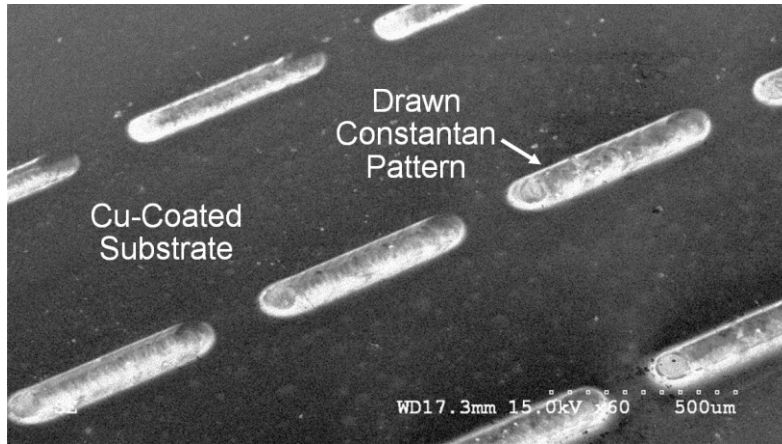
(a)



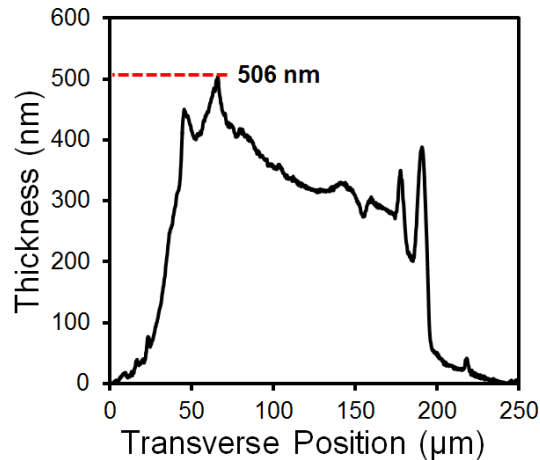
(b)

Figure 3-2 Results of fabrication of the T-Type thermocouple junction

(a) optical image of the micro Constantan electrode being scanned over the substrate, showing a micro glow plasma generated between them and a deposited film pattern, (b) optical image of a thermocouple device (Constantan film over copper layer) (upper) and SEM image of deposited surface (lower),



(a)



(b)

Figure 3-3 Results of Constantan drawing

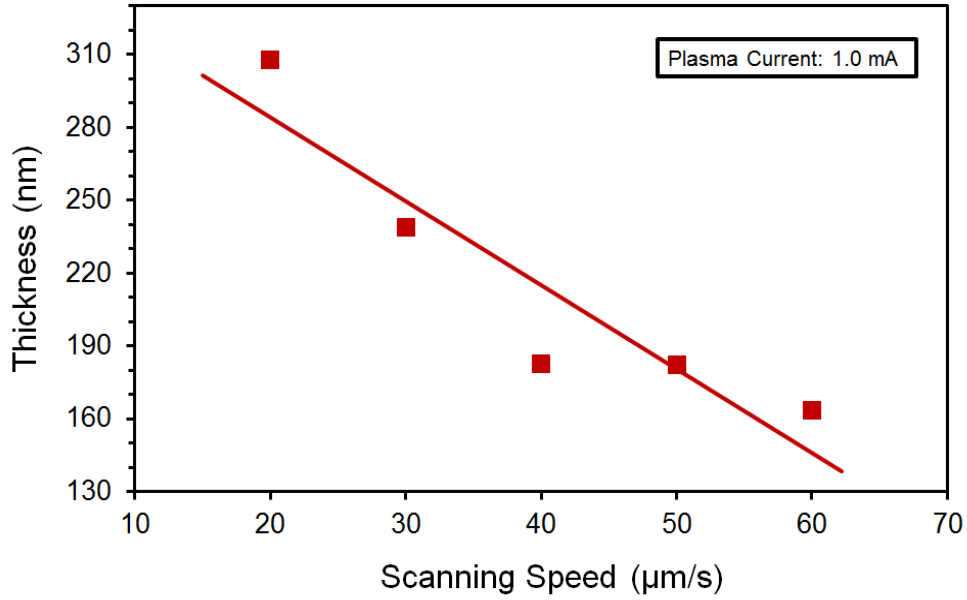
(a) SEM image of a produced array of Constantan line patterns (b) Cross-sectional profile of a linear pattern (printed at 1.0 mA and 50 μm/s)

The geometric dependence of the Constantan linear patterns on the process conditions was evaluated by varying the plasma current and the scanning speed (Figure 3-4) similar to what was done in section 2.3. As indicated in Figure 3-4(a), the clear tradeoff relationship between the film thickness and the electrode's scanning speed can be concluded. The average thickness was observed to change approximately from 330 nm to 170 nm by varying the scanning rate from 20 μm/s to 60 μm/s when the plasma current was 1.0 mA. The experiments also showed a dependence

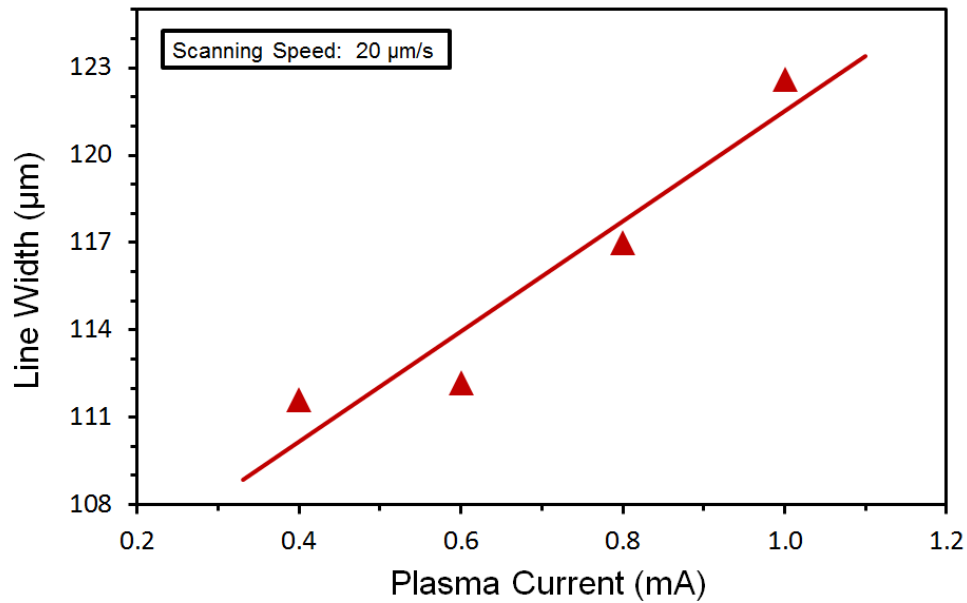
of the width of a printed line on the plasma current (Figure 3-4(b)). The line width was measured to widen (by 23% with an increase of the current from 0.4 mA to 1.0 mA, at a scanning rate of 60 $\mu\text{m/s}$) which is consistent to what was concluded from section 2.3.

3.3 Test Setup and Preliminary Test Results of T-Type Thermocouples

The micro-patterned Constantan-on-copper structures were tested to evaluate their effectiveness as thermocouples and their thermal responses using the set-up shown in Figure 3-5(a). As shown in the figure, test samples of the fabricated structures were placed on a heat source to vary their temperature from room temperature ($\sim 18^\circ\text{C}$) up to $\sim 100^\circ\text{C}$. This temperature range was enough to measure the Seebeck coefficient of the fabricated thermoelectric junction. The electrical connections to the sensing junction layers were made using wires of the same materials as the layers (Constantan and copper) to avoid any thermoelectric voltage built up at these contacts. The Constantan wire used as the sputtering target was used to probe the Constantan pattern (Figure 3-5(b)), and a commercial copper wire was connected to the top of the glass substrate (from the copper side). The device sample was heated while recording device temperature using a commercial thermocouple placed on the device substrate to probe its temperature directly, whereas the reference (cold) junction at which the two wires were coupled to a voltmeter was maintained at room temperature. The thermocouple voltage from the bilayer structures was clearly observable in the above set-up. Figure 3-6 plots a typical measured response of the voltage with temperature (obtained using the device with the same design as the one in the optical image of Figure 3-2(b)), showing a consistent temperature dependence of the voltage, with a sensitivity of $39\ \mu\text{V}/^\circ\text{C}$ that is close to the known Seebeck coefficient of the T-type thermocouple (approximately $40\text{-}46\ \mu\text{V}/^\circ\text{C}$ for the tested temperature range [62]). This preliminary test result experimentally verified the feasibility of micro thermocouple printing using the developed microplasma drawing process.

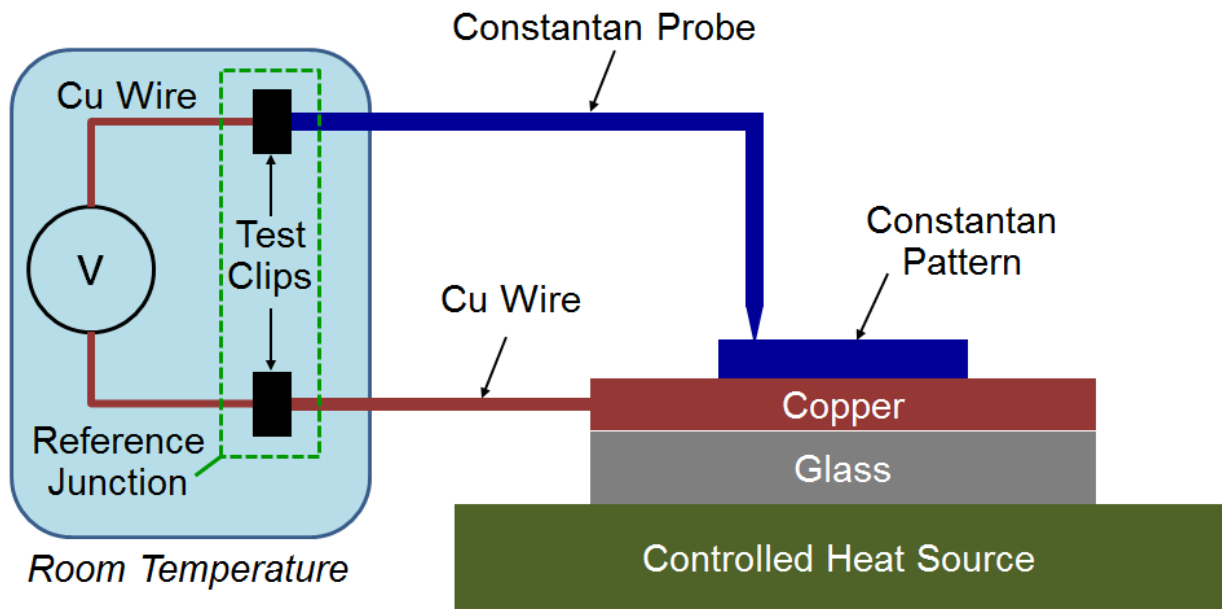


(a)

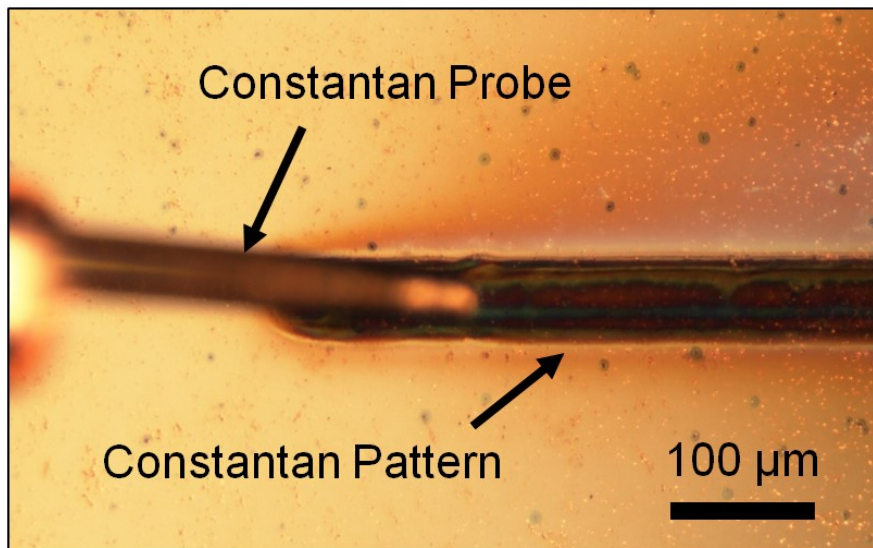


(b)

Figure 3-4 Characterization results of Constantan linear patterns created using 80- μm -diameter electrodes
(a) Film thickness (mean value along the transverse cross section of the pattern) vs. scanning speed (b) line width vs. plasma current. (Each data point is an average of five measurement results.)



(a)



(b)

Figure 3-5 Experimental set-up used to characterize printed micro thermocouples.

(a) Schematic (b) Optical image showing the 50- μm Constantan probe on a Constantan pattern.

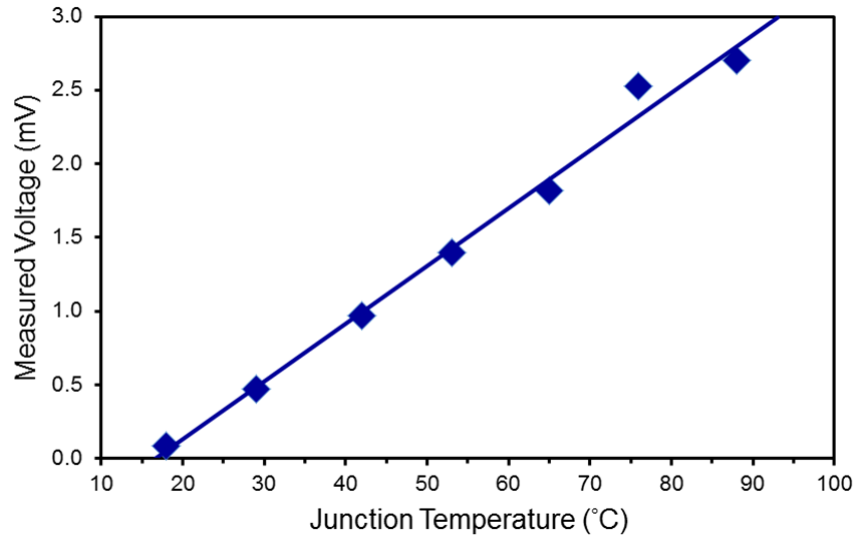


Figure 3-6 Measured thermocouple voltage as a function of temperature

3.4 An Approach towards a Fully Printed Micro-Thermocouple

The previous sections have demonstrated the ability to directly write Constantan alloy over copper-coated substrates to form a vertical T-Type thermocouple junction. However, a desired form to expand the degree of freedom in the design of such sensor device is that the thermocouple junction is created by patterning two corresponding metals/alloys on an insulator. In this section, an approach towards fully printed thermocouple sensors is discussed, in which both copper and Constantan films are patterned using the developed DC micro-sputtering technique. This section outlines the method to deposit these materials between two metal pads isolated on a dielectric surface and proves the feasibility of the proposed technique that is potentially usable for the device fabrication.

3.4.1 DC Micro-Sputtering Deposition on Insulators

Figure 3-7 shows the steps of fabrication of a fully printed T-type thermocouple device. Firstly, a thin film of silicon dioxide (~400 nm) is deposited on a low resistivity (0.001-0.005 Ω .cm) silicon substrate using electron-beam evaporator (Figure 3-7(a)). Next, chromium pads with thickness of

~400 nm are patterned on the oxide layer by means of electron beam evaporation and lift-off techniques (Figure 3-7(b)), after which the chromium layer is electrically short circuited to the substrate. The samples are then subjected to the direct-writing process to locally sputter the each thermocouple material by initiating the deposition from the pad location (Figure 3-7(c-d)).

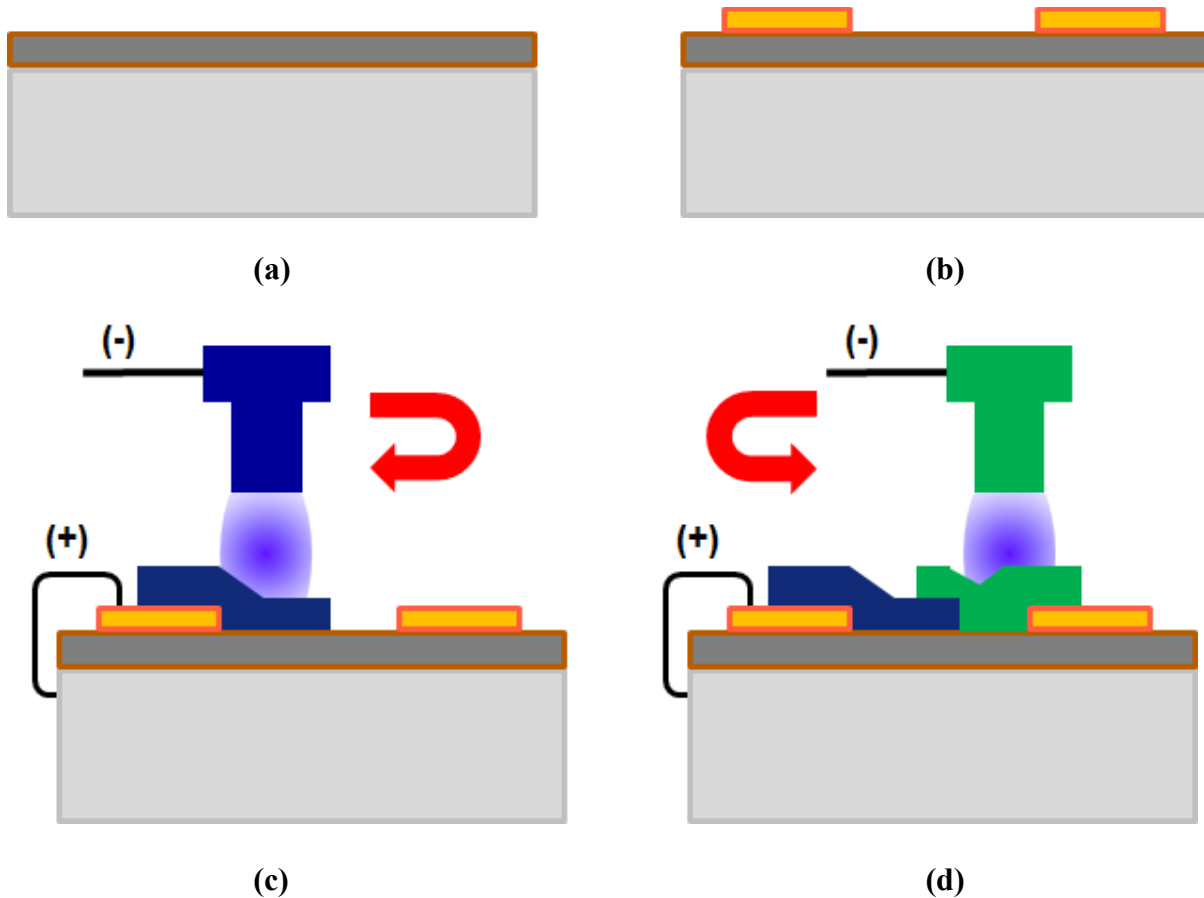


Figure 3-7 Fabrication process of a fully printed thermocouple

(a) Deposit a thin layer (~400 nm) of SiO₂ on the top of silicon substrate (b) pattern metal pads (chromium) on silicon dioxide using lift-off (c-d) micro-sputtering of the two thermocouple alloys to form the junction between the pads

3.4.2 Preliminary Patterning Results

Using the process described above, similar to the experiment in section 3.2, the micro glow plasma was verified to stably sustain on the electrode with discharge gaps of $\sim 10\ \mu\text{m}$ and deposit the material locally in both static and scanning modes. A sample structure, drawn using a $80\text{-}\mu\text{m}$ -diameter electrodes (at a plasma current of $1.2\ \text{mA}$ and a scanning rate of $20\ \mu\text{m/s}$) is shown in Figure 3-8. Both the Constantan and copper patterns are well defined to form a junction on the silicon-dioxide surface between the pads. Each line was patterned by scanning the microplasma 10 times to deposit a relatively thick film. It was observed that the deposition rate of both alloys was lower on the oxide region than on the pads, which may be attributed to the difference in electric field intensities on these regions. This preliminary testing proves the feasibility of patterning metals on insulator using the DC microplasma. Through further optimization, this technique could be applied to sensor patterning for a variety of thermocouple types.

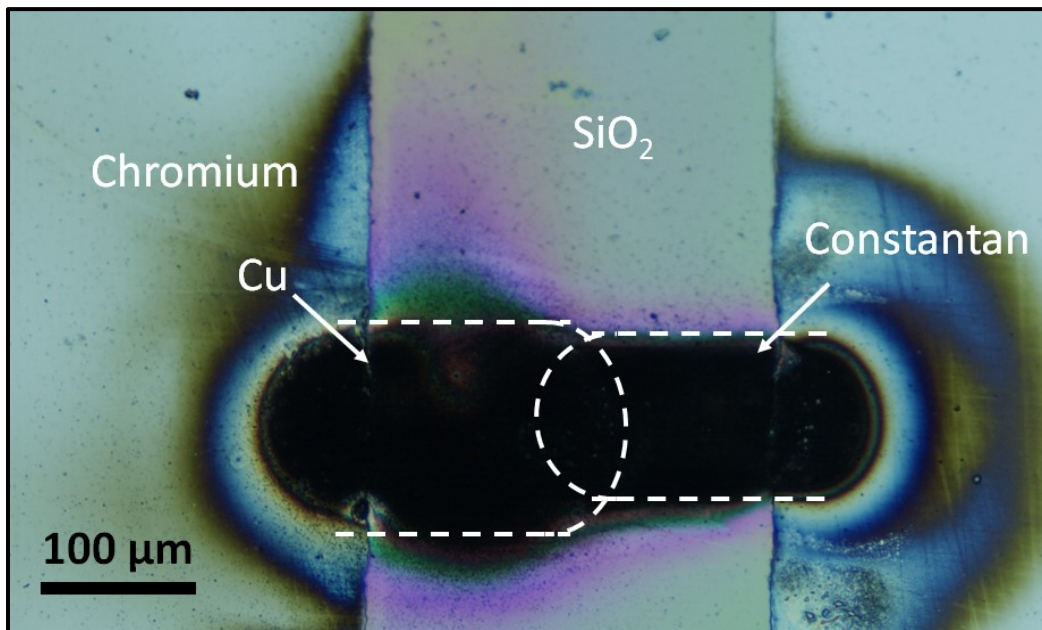


Figure 3-8 Optical microscope image of a patterned structure.

Chapter 4: Conclusion and Future Work

This thesis presented the research results obtained under an ongoing project in the Takahata Laboratory at the University of British Columbia, which is aimed at the development of a localized thin film deposition platform to enable direct writing of metallic thin films. The work has investigated the controlled deposition of metallic thin films via microplasma discharge scanning to fabricate the desired geometric patterns. Application of this process to thermocouple sensor printing was demonstrated.

4.1 Summary of the Research

A novel micro-sputter-deposition and direct writing method of metal films by manipulation of a micro glow plasma were presented. The sputtering was achieved by means of a highly confined microplasma discharge generated at a micro-machined electrode tip of the target material. The EDX and SEM analyses showed that the compositions of the film deposited using microelectrodes of specific alloys were consistent with those of the target materials, and that its surfaces were comprised of nanoparticles. The deposition of four different materials (pure copper, copper-tungsten alloy, nickel 200 alloy, and Constantan) was successfully validated. Direct film writing, performed by scanning the microelectrodes over silicon substrates, was experimentally characterized to reveal fine deposition with line widths down to 50 μm for both metals and metal alloys with thicknesses which are controllable with the electrode size, the discharge current, and the scanning speed. Patterning of microstructures on planar surfaces, as well as nonplanar substrates, was experimentally demonstrated. Out-of-plane writing of copper film was demonstrated towards the application to direct metal printing on 3D samples.

The application of the presented process to rapid micro-printing of thin-film thermocouple devices was explored. Direct writing of Constantan film, achieved by controlled scanning of micro glow plasma generated using micro-machined electrodes of the alloy over Cu-coated substrate, was experimentally characterized with a focus on patterning of T-type thermocouples. The thermoelectric measurement of printed microstructures revealed that they indeed functioned as temperature sensors with a sensitivity consistent with the typical coefficient of the particular thermocouple type, verifying the feasibility of the device concept.

The developed process is promising for rapid and low-cost production of thin-film patterns for a variety of microfabrication and packaging purposes through further optimization. The ability for thick film writing also offers its potential application to additive formation of 3D metal microstructures. Founded on a physical sputtering principle that allows deposition of many different alloys, through further optimization, the developed process could be extended to printing of a variety of thermocouples and thermopiles including those compatible with high temperatures, for their applications from temperature sensors to thermoelectric generators.

4.2 Future Work

Future work includes further optimization of the target electrode shape, using the wire-electro-discharge grinding to obtain the desired pattern geometry, especially when depositing over nonplanar surfaces. In addition parallel processing can be implemented by attaching an array of electrodes instead of one to increase the throughput of the process and speed-up multiple devices prototyping. The resolution of the process is determined by the size of the electrode, therefore different micromachining techniques which can achieve smaller sizes can be investigated. In case

of the characterization of the film properties, Electrical and optical characteristic parameters may be measured to ensure the material properties are as needed.

The discharge chamber may be better sealed to help eliminate the turbulent flow of nitrogen, as in the present case, which would help attain a more stable glow discharge. Having a sealed chamber will also enable the use of different sputtering gases which might extend the process to reactive gases and hence deposit different compounds. Although the proposed system is simple and of low cost, the study could also extend to vacuum environment and its dependence of patterning performance.

On the sensor's side, the development of a test setup of the micro-patterned thermocouple can be done by patterning a micro-heater wire over the junction by means of lithography to locally heat the junction and establish the temperature gradient required for thermoelectric voltage development. Different thermocouple alloys can be explored to develop temperature sensors for different environments. Printing of resistive temperature detectors (RTD) can be investigated as a complete temperature measurement device should have the thermocouple reference voltage corrected by means of RTD device [37]. Fabrication of temperature sensors on 3D microstructures that require thermal management such as smart implants or microfluidic channels is a promising research area to explore using the proposed direct-writing technique.

An important step is to work on the modeling of the micro-sputtered flux of particles which can be calculated on the basis of existing work done in [30], to study the film thickness profile and the electrode's consumption shape. The profile of the thin film cross section is one of the important parameters to test the process performance and product quality. The rate and the shape of the consumption of the electrode is important to optimize the electrode dimensions for a long target life time and a stable pattern geometry.

All the aforementioned improvements can be combined to realize an integrated printing platform for different materials on different types of substrates, without the need of complex systems.

Bibliography

- [1] V. Badilita, K. Kratt, T. Burger, J. G. Korvink and U. Wallrabe, "3D high aspect ratio, MEMS integrated micro-solenoids and Helmholtz micro-coils," in *Transducers*, , Denver, CO, USA, 2009.
- [2] Z. Yang, S. Uchiyama¹, Y. Zhang, M. Hayasei and T. Itoh, "3D microcoil fabricated on the capillary surface by cylindrical projection lithography for NMR Application," in *16th International Conference on Miniaturized Systems for Chemistry and Life Sciences*, Okinawa, Japan, 2012.
- [3] E. Jabari, S. A. A. Tong and E. Toyserkani, "Non-planar interconnects in double-sided flexible Cu-PET substrates using a laser-assisted maskless microdeposition process: 3D finite element modeling and experimental analysis," *Optic. Laser Eng.*, , vol. 54, p. 117–127, 2004.
- [4] B. Muralidharan and H. Chelladurai, "Experimental analysis of electro-discharge deposition process," *Int J Adv Manuf Technol*, vol. 76, p. 69–82, 2015.
- [5] Z. Wang, J. Cui and B. Jin, "Study on Micro Electrical Discharge Deposition in Air," in *2007 IEEE International Conference on Mechatronics and Automation*, Harbin, China, 2007.
- [6] J. Benedikt, K. Focke, A. Yanguas-Gil and A. v. Keudell, "Atmospheric pressure microplasma jet as a depositing tool," *Applied Physics Letters*, vol. 89, p. 251504, 2006.
- [7] L. Wee and L. Li, "Multiple-layer laser direct writing metal deposition in electrolyte solution," *Applied Surface Science*, vol. 247, pp. 285-293, 2005.
- [8] J. Chen, A. Palla-Papavlu, Y. Li, L. Chen, X. Shi, M. Döbeli, D. Stender, S. Populoh, W. Xie, A. Weidenkaff, C. W. Schneider, A. Wokaun and T. Lippert, "Laser deposition and direct-writing of thermoelectric misfit cobaltite thin films," *Applied Physics Letters*, vol. 104, p. 231907, 2014.
- [9] A. J. M. Mackus, J. J. L. Mulders, M. C. M. v. d. Sanden and W. M. M. Kessels, "Local deposition of high-purity Pt nanostructures by combining electron beam induced deposition and atomic layer deposition," *Journal of Applied Physics*, vol. 107, p. 116102, 2010.

- [10] A. Kamyshny, J. Steinke and S. Magdassi, "Metal-based Inkjet Inks for Printed Electronics," *The Open Applied Physics Journal*, vol. 4, pp. 9-36, 2011.
- [11] "Sputtering of Cu in a High Pressure Atmosphere," *Applied Surface Science*, vol. 33/34, pp. 1107-1113, 1987.
- [12] G. Mattana and D. Briand, "Recent advances in printed sensors on Foil," *Materials Today*, vol. 19, no. 2, pp. 88-99, 2016.
- [13] M. Ohring, *Materials Science of Thin Films: Depositions & Structure* 2nd Edition, San Diego: Academic Press Inc., 2002, p. 147.
- [14] Y. P. Raizer, *Gas Discharge Physics*, Berlin Heidelberg: Springer-Verlag, 1991.
- [15] J. L. Vossen and .. J. Cuomo, *Thin Film Processes*, New York: Academic Press, Inc., 1978.
- [16] J. L. Vossen and W. Kern, *Thin Film Processes II*, San Diego, CA: Academic Press, INC, 1991, p. 21.
- [17] V. A. Lisovskiy, S. D. Yakovin and V. D. Yegorenkov, "Low-pressure Gas Breakdown in Uniform DC Electric Field," *J. Phys. D*, vol. 33, pp. 2722-2730, 2000.
- [18] L. F. Berzak, S. E. Dorfman and S. P. Smih, "Paschen's Law in Air and Noble Gases," Engineering Division - Lawrence Berkeley National Laboratory, Berkeley, CA, 2006.
- [19] R. Cumeras, E. Figueras, C. E. Davis, B. J. I. and I. Gràciaa, "Review on Ion Mobility Spectrometry. Part 2: hyphenated methods and effects of experimental parameters," *Analyst*, vol. 140, no. 5, p. 1391–1410, 2015.
- [20] Duniway Stochroom Corporation, "Misc Data Sheets - Paschen's Curve," [Online]. Available: https://www.duniway.com/images/_pg/paschen-curve.pdf. [Accessed 18 November 2016].
- [21] D. Staack, B. Farouk, A. Gutsol and A. Fridman, "Stabilization of the ionization overheating thermal instability in atmospheric pressure microplasmas," *Journal of Applied Physics*, vol. 106, p. 013303, 2009.
- [22] G. Eden and S.-J. Park, "Sheetlike microplasmas have many applications," *Laser Focus World*, vol. 46, no. 7, p. 33–37, 2010.

- [23] A. D. Koutsospyros, S.-M. Yin, C. Christodoulatos and K. Becker, "Plasmochemical degradation of volatile organic compounds (VOC) in a capillary discharge plasma Reactor," *IEEE Transactions on Plasma Science*, vol. 33, no. 1, pp. 42-49, 2005.
- [24] C.-P. Klages, A. Hinze, P. Willich and M. Thomas, "Atmospheric-Pressure Plasma Amination of Polymer Surfaces," *Journal of Adhesion Science and Technology*, vol. 24, no. 6, p. 1167–1180, 2010.
- [25] D. Mariotti and R. M. Sankaran, "Microplasmas for nanomaterials synthesis," *J. Phys. D: Appl. Phys.*, vol. 43, no. 32, p. 323001, 2010.
- [26] C. Richmonds and M. Sankaran, "Plasma-liquid electrochemistry: rapid synthesis of colloidal metal particles by microplasma reduction of aqueous cations," *Appl. Phys. Lett.*, vol. 93, no. 13, p. 131501, 2008.
- [27] "Selective Deposition of Silicon at Room Temperature Using DC Microplasmas," *IEEE Transactions on Plasma Science*, vol. 35, no. 3, pp. 573-577, 2007.
- [28] S. A. Wright and Y. B. Gianchandani, "A harsh environment, multi-plasma microsystem with pressure sensor, gas purifier, and chemical detector,," in *2007 IEEE 20th International Conference on Micro Electro Mechanical Systems (MEMS)*, Hyogo, 2007.
- [29] P. Lindner and R. S. Besser, "A microplasma reactor for chemical intensification," *Chemical Engineering & Technology*, vol. 35, no. 7, p. 1249, 2012.
- [30] Z. Yichena, S. Qingzhu and S. Zhulaib, "Research on Thin Film Thickness Uniformity for Deposition of Rectangular Planar Sputtering Target," *Physics Procedia*, vol. 32, p. 903 – 913, 2012.
- [31] J. E. Mahan, *Physical Vapor Deposition of Thin Films*, New York: John Wiley & Sons, Inc., 2000.
- [32] D. V. Ho, "The Design and Modification of a Sputter System for DC Reactive Sputterign of Alumina and Zirconia Thin Films," MSc thesis, Louisiana State University, LA, 2011.
- [33] A. L. Gobbi and P. A. P. Nascente, "D. C. Sputtering," in *Encyclopedia of Tribology*, Springer US, 2013, pp. 699-706.
- [34] R. Wendt and K. Ellmer, "Desorption of Zn from a growing ZnO:Al-film deposited bymagnetron sputtering," *Surf. Coat. Tecnol*, vol. 93, no. 27, 1997.

- [35] M. J. Madou, *Manufacturing Techniques for Microfabrication and Nanotechnology*, 3rd ed., vol. II, New York: CRC Press, 2011.
- [36] H. Tawara and Y. Yamamura, "Energy Dependence of the Yields of Ion-Induced Sputtering of Monatomic Solids," *Atomic Data and Nuclear Data Tables*, vol. 62, no. 2, pp. 149-253, 1996.
- [37] Omega Corporation, "Introduction to Thermocouples and Thermocouple Assemblies," [Online]. Available: <http://www.omega.com/temperature/pdf/thermocouple.pdf>. [Accessed 17 November 2016].
- [38] S. M. Peters, "Thermocouple Temperature Measurements for Twin Jet Thermal Mixing," MSc thesis, The University of Tennessee, Knoxville, Tennessee, 2011.
- [39] T. W. Kerlin and R. L. Shepard, *Industrial temperature measurement*, Research Triangle Park, NC: Instrument Society of America, 1982.
- [40] S. O. Kasap, "Thermoelectric Effects in Metals: Thermocouples," University of Saskatchewan, Canada, 2001.
- [41] T. Masuzawa, M. Fujino, K. Kobayashi, T. Suzuki and T. Kinoshita, "Wire electro-discharge grinding for micro-machining," *Ann. CIRP*, vol. 34, p. 431–434, 1985.
- [42] R. K. Tiwari, S. Kumar and G. R. Mishra, "A High Performance Novel PMOS Wilson Current Mirror," *International Journal of Electronics Engineering*, vol. 4, no. 2, pp. 173-176, 2012.
- [43] B. Razavi, *Design of Analog CMOS Integrated Circuits*, 5th ed., Mc Graw Hill, 2001.
- [44] K. Smith and A. Sedra, *Microelectronic Circuits*, 6th ed., Oxford Press, 2009.
- [45] C. Moreau, P. Fargier-Richard, R. G. Saint-Jacques and P. Cielo, "Thermal diffusivity of plasma-sprayed tungsten coatings," *Surface and Coatings Technology*, vol. 61, no. 1, pp. 67-71, 1993.
- [46] S. D. Tanner, "Plasma temperature from ion kinetic energies and implications for the source of diatomic oxide ions in inductively coupled plasma mass spectrometry," *Journal of Analytical Atomic Spectrometry*, vol. 8, no. 6, pp. 891-897, 1993.

- [47] S. Ayoub and L. Y. Beaulieu, "The surface morphology of thin Au films deposited on Si(001) substrates by sputter deposition," *Thin Solid Films*, vol. 534, pp. 54-61, 2013.
- [48] H. Wei and H. Eilers, "From Silver Nanoparticles to Thin Films: Evolution of Microstructure and Electrical Conduction on Glass Substrates," *Journal of Physics and Chemistry of Solids*, vol. 70, p. 459–465, 2009.
- [49] G. E. Totten, K. Funatani and L. Xie, *Handbook of Metallurgical Process Design*, New York: CRC Press, 2004.
- [50] K. Oura, M. Katayama, A. V. Zotov, V. G. Lifshits and A. A. Saranin, "Surface Science: An Introduction," in *Elementary Processes at Surfaces II. Surface Diffusion*, Springer, 2003, pp. 325-356.
- [51] K. Bordo and H.-G. Rubahn, "Effect of Deposition Rate on Structure and Surface Morphology of Thin Evaporated Al Films on Dielectrics and Semiconductors," *Materials Science*, 2012.
- [52] F. T. Toth, F. G. Rammerstorfer, M. J. Cordill and F. D. Fischer, "Detailed modelling of delamination buckling of thin films under global tension," *Acta Materialia*, vol. 61, no. 7, pp. 2425-2433, 2013.
- [53] C. Coupeau, P. Goudeau, L. Belliard, M. George, N. Tamura, F. Cleymand, J. Colin, B. Perrin and J. Grilhé, "Evidence of plastic damage in thin films around buckling structures," *Thin Solid Films*, Vols. 469–470,, p. 469–470, 2004.
- [54] R. Cornely, "Film growth by ion beam and plasma discharge sputtering method,," in *in Ion Beam Assisted Film Growths*, T. Itoh, Ed., Amsterdam, Elsevier, 1989, pp. 9-32.
- [55] D. Newbury, "Mistakes encountered during automatic peak identification of minor and trace constituents in electron-excited energy dispersive X-ray microanalysis," *Scanning*, vol. 31, no. 8, p. 91–101, 2009.
- [56] H. Tanaka, S. Yamashita, Y. Abe, M. Shikida and K. Sato, "Fast wet anisotropic etching of Si{100} and {110} with a smooth surface in ultra-high temperature KOH solutions," in *12th International Conference on Solid-State Sensors, Actuators and Microsystems*, Boston, MA, 2003.

- [57] P. Alvi, V. Meel, K. Sarita and J. Akhtar, "A Study on Anisotropic Etching of (100) Silicon in Aqueous KOH Solution," *Int. J. Chem. Sci*, vol. 6, no. 3, pp. 1168-1176, 2008.
- [58] E. D. Palik, O. J. Glembocki, I. H. Jr, P. S. Burno and L. Tenez, "Etching roughness for (100) silicon surfaces in aqueous KOH," *Journal of Applied Physics*, vol. 70, pp. 3291-3300, 1991.
- [59] K. Becker, U. Kogelschatz, K. Schoenbach and R. Barker, *Non-Equilibrium Air Plasmas at Atmospheric Pressure*, vol. 29, Ringgold Inc, 2005.
- [60] L. Rebenklau, P. Gierth, A. Paproth, K. Irrgang, L. Lippmann, A. Wodtke, L. Niedermeyer, K. Augsburg and F. Bechtold, "Temperature sensors based on thermoelectric effects," in *Eur. Microelectron. Packag. Conf.*, 1-5, 2015.
- [61] J. Courbat, Y. B. Kim, D. Briand and N. F. d. Rooij, "Inkjet printing on paper for the realization of humidity and temperature sensors," in *Int'l Solid-State Sensor. Actuator. Microsyst. Conf.*, 2011.
- [62] M. Duff and J. Towey, "Two ways to measure temperature using thermocouples feature simplicity, accuracy, and flexibility," *Analog Dialogue*, vol. 44, no. 10, p. 1–6, 2010.

Appendix A: Wet Potassium Hydroxide (KOH) Etching of Silicon

To prepare the silicon steps in Figure 2-11 and Figure 2-12(b), masks of SU-8 and silicon nitride respectively were used in the wet etching processes. The silicon steps were prepared by etching silicon in a hot KOH solution ($\sim 140^\circ\text{C}$, 50 gm KOH, and 60 ml DI water) to achieve both a fast etching speed ($\sim 10\mu\text{m}/\text{minute}$) and smooth surfaces [56, 57, 58]. For the samples in Figure 2-11, as shown in Figure A-1, SU-8 2015 negative photoresist was spin-coated at 4000 rpm, patterned, and developed over the silicon substrate directly. A 30-minute post baking step was used to harden the mask. After that, the samples were immersed in KOH solution for 1-2 minutes to perform the anisotropic etching of silicon to a depth of $\sim 10\mu\text{m}$. The etched silicon (with SU-8 on top) was then put in diluted hydrofluoric acid (10% wt. HF) to remove the SU-8 mask.

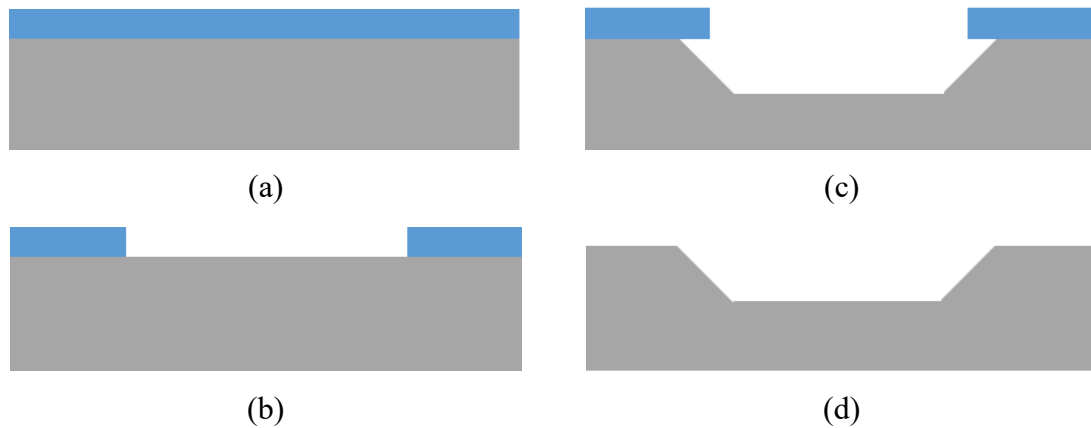


Figure A-1 Process steps of wet-etching of silicon with SU-8 mask.

(a) spin coating of SU-8 on silicon; (b) SU-8 mask after exposure and development; (c) etching of silicon in KOH solution; (d) striping of SU-8 in HF solution

The SU-8 mask was attacked by the KOH solution at the used temperature (see the rounded corners in Figure 2-11 which were done using a square mask). Therefore, to achieve deeper etching for the case in Figure 2-12(b), a hard mask (like silicon nitride) was required. As shown in Figure A-2, 300 nm layer of silicon nitride was deposited using a Trion PECVD system by flowing silane (SiH_4), ammonia (NH_3), and nitrogen (N_2) gases at ratios 3:40:10 at chamber pressure of 500 mTorr. AZ P4110 positive photoresist was spin-coated and patterned to create an etching mask for the nitride layer. Next, the nitride film was etched in oxygen plasma until the silicon was exposed.

The silicon samples with patterned nitride mask was then immersed in the same KOH solution for 6-8 minutes. The etched silicon was then rinsed in 30% BOE solution to remove the nitride mask.

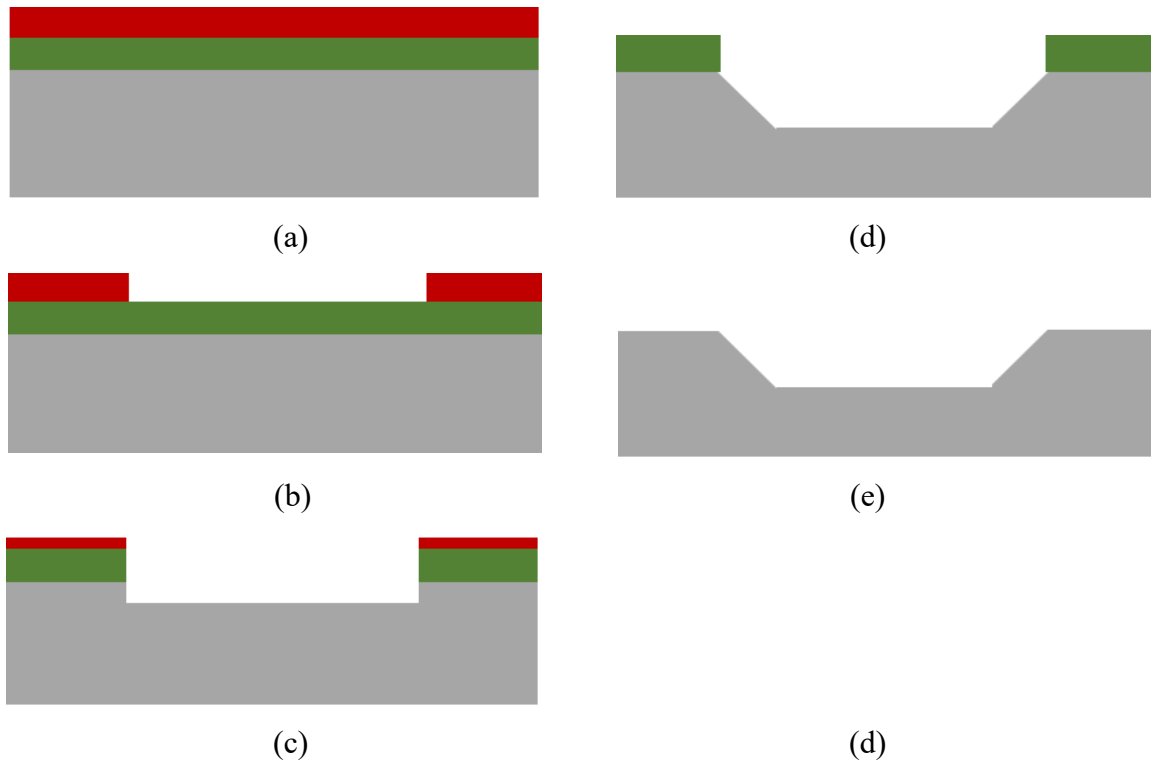


Figure A-2 Process steps of wet-etching of silicon with PECVD silicon nitride mask.

(a) PECVD deposition of silicon nitride (~300nm) and spin coating of AZ P4110 on silicon; (b) photoresist after exposure and development; (c) plasma etching of nitride mask; (d) etching of silicon in KOH solution; (e) removing of nitride mask in BOE solution